

Highly nonlinear $\text{Pb}_2\text{P}_2\text{O}_7\text{-Nb}_2\text{O}_5$ glasses for optical fiber production

Danilo Manzani^{1}, Tiago Gualberto², Juliana M. P. Almeida², Murilo Montesso³, Cléber R. Mendonça², Victor A. G. Rivera², Leonardo De Boni², Marcelo Nalin¹, Sidney J. L. Ribeiro¹*

¹ Instituto de Química – Universidade Estadual Paulista - UNESP, CP 355, 14801-970

Araraquara, SP, Brazil

² São Carlos Institute of Physics, University of São Paulo – USP, São Carlos, SP, Brazil

³ Department of Chemistry, São Carlos Federal University, UFSCar, São Carlos, SP, Brazil

Corresponding Author

*Dr. Danilo Manzani

São Paulo State University – UNESP - Institute of Chemistry

CP 355 - Araraquara, SP – Brazil

E-mail: danilo.manzani@gmail.com

Abstract

In this study we present the production and characterization of $\text{Pb}_2\text{P}_2\text{O}_7\text{-Nb}_2\text{O}_5$ glasses and optical fibers. The dependence of Nb_2O_5 content on thermal, structural and optical properties were investigated by thermal analysis (DSC), Raman spectroscopy, UV-Visible absorption, M-Lines and Z-scan techniques. Glass transition temperatures (T_g) increased linearly with Nb_2O_5 content up to 60 mol %, while thermal stability against crystallization (ΔT) reached a maximum value of 225 °C at 40 mol% of Nb_2O_5 . Raman spectra showed a significant structural change by the insertion of NbO_6 octahedral units in the glass network. The increase of Nb_2O_5 concentration shifts the glasses absorption edge to lower energies, and also increase the linear refractive indexes (n_0) due to the high polarizability of niobium atoms and formation of non-bridging oxygen. Similarly to n_0 , an increase in the positive values of nonlinear refractive indexes was observed using Z-Scan technique with increase of Nb_2O_5 content, based on structural changes caused by the replacement of $\text{Pb}_2\text{P}_2\text{O}_7$ instead Nb_2O_5 . The average of n_2 values at 500 – 1500 nm raised from 2.2×10^{-19} to $3.8 \times 10^{-19} \text{ m}^2/\text{W}$, when the Nb_2O_5 content was increased from 10 to 60 mol %. Lastly, a core-cladding preform was produced by suction method and the optical fiber drawn. The sample containing 40 mol% of Nb_2O_5 was used for presenting the highest thermal stability against crystallization and n_0 values greater than 2 from green to near-infrared wavelengths. Multimode step index fiber with good core circularity and concentricity was produced and the optical losses were determined by cut-back method at visible and near-infrared ranges.

1. Introduction

Lead pyrophosphate glasses containing tungsten oxide in the binary system $\text{Pb}_2\text{P}_2\text{O}_7\text{--WO}_3$ have already been investigated and shown interesting thermal and optical properties, resulting chemically stable, extremely high resistance against devitrification and high linear and nonlinear refractive indexes [1,2]. The optical properties were correlated with the specific phosphate glass network containing lead atoms and tungsten octahedrons. At high WO_3 contents the octahedrons WO_6 units linked together through W–O–W bonds to form highly polarizable clusters, which were pointed out to be responsible, in conjunction with lead atoms polarization, for high linear and nonlinear optical properties [2]. Besides the interesting optical properties, lead pyrophosphate glass present high vitrifying ability and unusual capability to dissolve large amounts of others glass formers, modifiers, or intermediate compounds without reduction of glass forming ability [3,4], as observed by the insertion of WO_6 inside the phosphate covalent network that form strong P–O–W bonds which are responsible to enhance the network connectivity [5].

Transparent phosphate glasses containing heavy metal oxides such as Bi_2O_3 , Sb_2O_3 , WO_3 , Nb_2O_5 , and PbO are subject of intense studies and widely exploited as optical components. In addition to the extended transparency window commonly up to 4 μm [9-13], ultrafast nonlinearity is also observed due to their nonlinear optical properties supported by the large polarizability of atoms with empty d orbitals (e.g. Ti^{4+} , Nb^{5+} , W^{6+}) or heavy cationic ions with an electronic configuration with ns^2 lone pair (e.g. Te^{4+} , Bi^{3+} , Sb^{3+} , Pb^{2+}) [6-9].

Poor chemical durability of most phosphate glasses is mainly due to the presence of [P–O] linkages, which easily adsorbs hydroxyl groups from environmental water. This feature limits their optical applications and has almost discouraged their further development as photonic

devices. However, the introduction of transition metal oxide such as WO_3 , Nb_2O_5 , MoO_3 and TiO_2 , which have several different oxidation states and high coordination number at high concentrations, gives glass formation features when combined with others glass former compound, increasing mechanical and chemical stability [14,15]. Notably, niobium phosphate glasses might be used in a varied range of applications, such as rare-earth ion hosts for laser materials, optical fibers, lenses, optical switches, electrodes and others photonics devices [16-18]. Teixeira et al. have studied the $\text{Na}_2\text{O}-\text{Al}_2\text{O}_3-\text{TiO}_2-\text{Nb}_2\text{O}_5-\text{P}_2\text{O}_5$ glass system and have demonstrated that niobium oxide is more effective than titanium oxide to improve refractive index properties and chemical durability of phosphate glass [19].

In this sense, the present work shows the study of thermal, structural and optical properties of the binary glass system $\text{Pb}_2\text{P}_2\text{O}_7-\text{Nb}_2\text{O}_5$ as a potential optical material for nonlinear applications. Linear optical properties were studied via absorption spectra and refractive index via direct and indirect optical band gap, Urbach energy and Sellmeier equation. Nonlinear optical properties were investigated by the Z-scan method to reinforce the application of these glasses as photonic materials. Further, the role of niobium oxide on glass forming ability and thermal stability was shown and the more stable composition was chosen to manufacture step-index preform and fibers by using the suction method. This method was already detailed described and used for allowing fabrication of core-cladding preform and optical fibers with good core-cladding interface and core circularity [20]. The main propose is the impact of the preform production method, e.g. the suction method, and the study of core-cladding interface and diameters for niobium lead-pyrophosphate glasses obtained as multimode optical fibers. The optical fiber was characterized regarding their structure by using optical microscopy and optical loss by cut back method, proving the photonic potential of this glass composition for optical

applications, either as bulk sample and optical fiber. The possibility of fabrication of fiber with strong light confinement due to the high linear refractive indices makes niobium pyro-phosphate glasses very competitive for photonic devices.

2. Experimental

2.1. Bulk glass synthesis

The glass samples were synthesized by the conventional melt-quenching method using the raw materials Nb_2O_5 (Aldrich 99.8%) and lead orthophosphate PbHPO_4 prepared by precipitation of a lead salt solution with pure orthophosphate acid at room temperature, as detailed describe in [1]. Chemicals were weighted for compositions $(100-x)\text{Pb}_2\text{P}_2\text{O}_7-x\text{Nb}_2\text{O}_5$ for $x = 10, 20, 30, 40, 50$ and 60 mol % and heated at 200°C for 1 h to reduce adsorbed water and gases under room atmosphere, since the PbHPO_4 is obtained via a wet chemical route. Then, the batch was melted under open air at a temperature ranging from 950 to 1200°C , depending on the Nb_2O_5 content for 40 minutes to ensure homogenization and fining. Finally, the melt was cooled inside a metal mould preheated at 20°C below the glass transition temperature, T_g , and then annealed at these temperatures for 2 h to minimize mechanical stress resulting from thermal gradients upon cooling. For a better readability, the glasses were labeled as shown in Table 1. The bulk glass samples of very good optical quality were finally polished for optical characterizations.

2.2. Bulk glass characterization

Glass characteristic temperatures such as glass transition temperature, T_g , onset crystallization temperature, T_x , and maximum of crystallization peak, T_p , were obtained from differential scanning calorimetry in the range of 300 to 1000°C using a NETZSCH equipment

DSC 404 F3 Pegasus calorimeter, with a maximum error of ± 2 °C for T_g and T_x (obtained from tangents intersection) and ± 1 °C for T_p . Glass pieces of about 12 mg were set in opened platinum pans under N_2 atmosphere and a heating rate of 10 °C/min.

Absorption spectra of the glasses samples were acquired from 200 to 800 nm with a Varian Cary 5000 spectrophotometer. Raman scattering spectra were acquired at room temperature in the frequency range from 150 to 1400 cm^{-1} by using a HORIBA Jobin Yvon model LabRAM HR micro Raman apparatus equipped with a 632.8 nm laser delivering 30 mW power.

Refractive indices were measured at three wavelengths (532, 632.8 and 1550 nm) by the prism-coupler technique (M-Lines) with a Metricon-2010 instrument using a prism with refractive indices from 1.7 to 2.45 and an precision of ± 0.0001 . Finally, the spectra of nonlinear refractive index were obtained by refractive (closed aperture) Z-scan technique using femtosecond laser pulses.

Z-scan technique was applied to obtain the third-order optical properties, represented by nonlinear absorption and nonlinear refraction. In the refractive Z-scan method (closed aperture), the sample transmittance passing through a tiny circular aperture, placed in the far field, is monitored while the sample is translated along the z axis of a focused Gaussian beam. As the sample approaches the focus, the light intensity increased leading to the self-focus effect (for a positive nonlinear index of refraction), and therefore changing the monitored signal as a function of sample position. By fitting the experimental data according to Sheik-Bahae model [21], the nonlinear index of refraction (n_2) could be obtained according to equation 1:

$$T(z, \Delta\phi_0) = 1 + \frac{4\Delta\phi_0 x}{(x^2 + 9)(x^2 + 1)} \quad (\text{Eq. 1})$$

where $\Delta\phi_0$ is the one-axes phase shift defined as $\Delta\phi_0 = kn_2 I_0 L$, in which I_0 is the on-axis irradiance at focus, L is the sample effective thickness, $\mathbf{k} = 2\pi/\lambda$ is the wave vector, λ is the laser wavelength, w_0 is the beam waist, and $\mathbf{x} = \mathbf{z}/z_0$, where z is the sample position, $z_0 = kw_0^2/2$ is the diffraction length of the beam. Removing the tiny aperture, the z-scan method enable to evaluate the nonlinear absorption (open aperture configuration) [22], represented herein by two photon absorption coefficient (β), which is determined from the experimental data through equation 2, assuming a temporal Gaussian pulse profile.

$$T = \frac{1}{\sqrt{\pi}q_0(z,0)} \int_{-\infty}^{\infty} \ln[1 + q_0(z,0)e^{-\tau^2}] d\tau \quad (\text{Eq. 2})$$

where, $q_0(z,t) = \beta I_0(t)L(1 + z^2/z_0^2)^{-1}$. Using a dual arm setup, close and open z-scan signatures were obtained simultaneously, and the effects of two photon absorption over nonlinear refraction have been deducted thought the ratio of both signatures.

For z-scan measurements, a Ti:sapphire chirped pulse amplified system (150-fs, 775 nm and 1 kHz) was used as the excitation source for an optical parametric amplifier, which provides 120-fs pulses from 460 up to 2000 nm, enabling to investigate the optical nonlinearities in a wide wavelength range. Depending on the excitation wavelength, the pulse energy and beam waist ranged from 4 –200 nJ and 12 to 29 μm , respectively. The experimental error for such measurements is approximately 15%, which is based on standard deviation and measurements of fused silica as reference material. Additional information about the experimental setup can be found in the literature [8,23].

2.3. Core-cladding preform and optical fiber fabrication

The specific literature reports different techniques applied for fabrication of heavy metal oxide glasses preforms of core-cladding optical fibers, such as: (i) double crucible method [24], (ii) rod in tube technique [25], and (iii) rotational casting processes, developed by Tran et al. in 1982 for fluoride-based fibers [26]. However, in this work we have used the *suction method*, which is fully detailed in [20] and following similarly principle to the setup described by Clarke in 1992 [27].

Core and cladding glasses compositions were also prepared by the conventional melt-casting method. Firstly, the raw materials of both compositions were weighed in order to obtain a 20.0 g core glass and a 40.0 g cladding glass, whose molar composition were $57\text{Pb}_2\text{P}_2\text{O}_7-43\text{Nb}_2\text{O}_5$ and $60\text{Pb}_2\text{P}_2\text{O}_7-40\text{Nb}_2\text{O}_5$, respectively. For better readability, the optical fiber host glasses are labeled P5.7N4.3 for core and P6N4 for cladding. A small larger amount of niobium oxide concentration (3 mol %) in the core composition is enough to increase its linear refractive index without affecting the mechanical and thermal properties. After mixing the raw materials by using a mixer machine model Speed Mixer (FlackTek, Inc.) at 2000 rpm by 1 minute, the batches were melted in a Pt/Au crucible at 1100 °C during 2 h in a conventional furnace and swelled every 20 minutes at room atmosphere to ensure complete decomposition of the lead pyrophosphate and good homogenization and fining [1].

The next step was to cast the melts into a special cylindrical stainless steel mold with 10.11 mm of internal diameter and preheated at 75 °C below glass transition temperature into a vertical electric furnace. The mold is equipped with a piston which has a downward movement along the cylinder revolution axis and detailed methodology to obtain core-cladding preform by *suction method* is described in [20]. For phosphate based glasses, this method allows the

fabrication of preforms from 50 to 100 mm in length and around 10 mm in diameter with good core-cladding interface quality and core circularity. Some special care during the preform fabrication were taken in order to minimize the formation of defects which would be present afterwards in the resulted fiber, such as: (i) use long melting time of 1 hour with periodic swirling every 15 minutes to ensure complete decomposition of PbHPO_4 to $\text{Pb}_2\text{P}_2\text{O}_7$ and to allow good homogenization and fining [1]; (ii) increase the batch viscosity before casting by reducing the melting temperature of about 100 °C in order to reduce crystallization tendency considering the low melting viscosity; and (iii) apply adequate annealing below glass transition temperature and slow cooling down to room temperature to minimize as much as possible residual internal stress and avoid the formation of micro cracks.

Finally, the annealed and cooled preform was pulled down using an optical fiber drawing tower and the step index optical fiber was fabricated. The drawing temperature for this preform was experimentally found by increasing the temperature at $T_g + 150$ °C and then adjusting the optimum temperature for drawing process by using a heating rate of 10 °C until reach the working temperature of 715 °C. The tower furnace temperature is controlled by an internal thermocouple placed close to the heating zone and purged with dry nitrogen at 2 L/min. Note that the fiber was obtained without polymeric coating and its mechanical strength is good enough to be handled. Nonetheless, our facilities allow us to cover the fiber with a protective polymeric layer for application which requires higher mechanical strengths. The cut-back method was employed to measure the propagation losses of the fiber over a length of about 30 cm.

3. Results and discussions

The glass samples present good optical quality and their color vary from transparent to brownish with the increase of Nb_2O_5 concentration as shown in Figure 1. The samples were

optically homogeneous under naked eyes and free of strains, which were avoided by using high melting temperature, large melting time, periodic swell and low cooling rates. X-ray diffraction patterns presented the typical amorphous halo for all compositions.

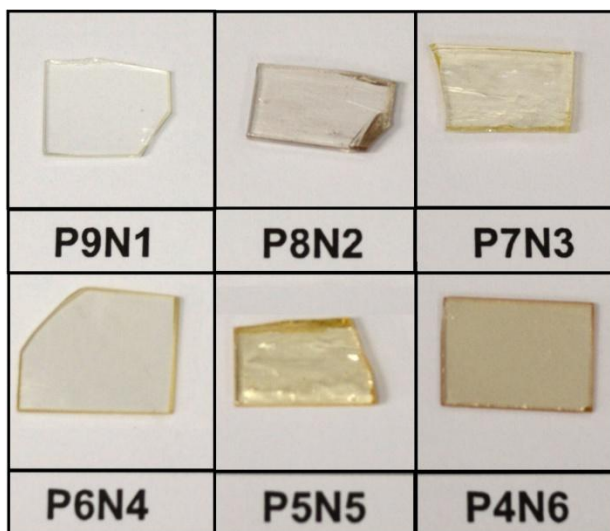


Figure 1. Photograph of the bulk glassy samples obtained from the binary system $(100-x)\text{Pb}_2\text{P}_2\text{O}_7 - x\text{Nb}_2\text{O}_5$ with $x = 10, 20, 30, 40, 50$ e 60 mol %.

Thermal characterization

In order to investigate the thermal properties of $\text{Pb}_2\text{P}_2\text{O}_7\text{-Nb}_2\text{O}_5$ glasses, DSC measurements were performed to obtain the characteristics temperatures showed in Table 1. Increasing the Nb_2O_5 content, the value of T_g increases up to the highest concentration of 60 mol % (P4N6). Glass thermal stability against crystallization was evaluated by using the thermal stability parameter ΔT , defined by $T_x - T_g$, which increases up to 40 mol % of Nb_2O_5 .

Table 1. Molar composition of the glassy samples and their characteristic temperatures.

Sample label	Pb ₂ P ₂ O ₇ (mol%)	Nb ₂ O ₅ (mol%)	T_g (°C)	T_x (°C)
P9N1	90	10	427 ± 2	524
P8N2	80	20	467 ± 2	598
P7N3	70	30	526 ± 2	704
P6N4	60	40	555 ± 2	807
P5N5	50	50	568 ± 2	756
P4N6	40	60	592 ± 2	700
Core	60	40	555 ± 2	807
Cladding	57	43	559 ± 2	803

Figure 2 shows the evolution of the glass transition temperature and the ΔT ($T_x - T_g$) parameter varying Nb₂O₅ concentration from 10 to 60 mol %. The T_g presented an enhancement from 427 °C to 592 °C, which can be understood by the increasing of network connectivity (polymerization process), making them more rigid up to 60 mol % of Nb₂O₅ due to the insertion of NbO₆ octahedral units into the glass network. It means that niobium atoms enhance the covalent character of the glass network and acts similarly as usual glass former compounds in the glassy samples. Similar behavior was already demonstrated in the binary system Pb₂P₂O₇–WO₃, varying WO₃ concentration, which has been also related with an increase of the network connectivity due to WO₆ octahedral units insertion into the lead phosphate chains [1,14]. In addition, the samples present good thermal stability against crystallization, with ΔT values above 100 °C up to ~ 250 °C, as seen in Figure 2.

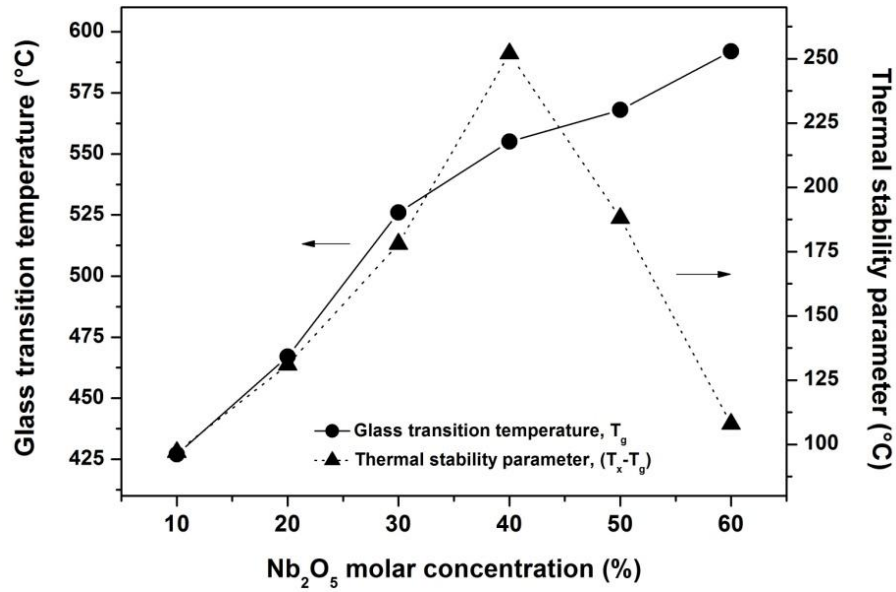


Figure 2. Behavior of the glass transition temperature (closed circles) and the thermal stability parameter $\Delta T = T_x - T_g$ (closed triangles) as function of Nb_2O_5 concentration. The lines are just a guide to the eyes and the measure error is $\pm 1^\circ\text{C}$.

Thermal stability against crystallization showed a two-step behavior, as illustrated in Figure 2: (i) up to 40 mol % of Nb_2O_5 an increase of ΔT is clearly observed from 97 to 252 °C since the crystallization peak is shifted to higher temperatures. This behavior is consistent with the increase of network connectivity (increase of T_g). Pure pyrophosphate glasses have high crystallization tendency owing to their small chains size, resulting low viscosity above glass transition temperature. Thus, the incorporation of niobium oxide allowed obtains highly stable glasses with maximum thermal stability of 252 °C for P6N4 glass sample, indicating the potentiality of that based composition to produce optical fibers, since the preform fabrication and drawing process need high thermal stability compositions and high viscosities above T_g , which is known to difficult structural reorganization and crystallization; and (ii) above 40 mol %, the addition of niobium oxide leads to a decrease of thermal stability from 252 to 108 °C, which may

be related to the breaking of niobium lead polyphosphate chains, nucleation of NbO_n clusters at high concentrations or saturation of Nb_2O_5 amount soluble into lead pyrophosphate matrix. However, the T_g increases above P6N4 glass sample, indicating any network chains modification. In this sense, the behavior from 40 to 60 mol % of Nb_2O_5 can be understood due to the shift of crystallization peak to low temperatures as larger the concentration of niobium oxide and, consequently due to the formation of NbO_n clusters, which are assigned by the appearance of Nb–O–Nb Raman band at Raman frequency as explained below.

Raman spectroscopy

Figure 3 shows Raman spectra from 150 to 1400 cm^{-1} obtained for the glass samples and chemicals $\text{Pb}_2\text{P}_2\text{O}_7$ and Nb_2O_5 . The Raman spectrum of lead pyrophosphate precursor present the main bands at 720, 1013 and 1115 cm^{-1} , attributed to P–O–P linkages in $(\text{P}_2\text{O}_7)^{4-}$ units, symmetric and anti-symmetric stretching vibration of Q^1 phosphate tetrahedral, respectively. The polymorphism of niobium oxide has been reported before with NbO_n polyhedra arranged in different complex structures [30,31]. The phase transformation strongly depends on the heat treatment from 300°C to 1000°C and the niobium oxide increases in degree of crystallinity to form more stable Nb_2O_5 phases [32]. Since the glass samples were produced using melting temperatures above 1000 °C, at this temperature the preferential phase of niobium oxide precursor is the H- Nb_2O_5 phase, and it is the most thermodynamically stable form among the Nb_2O_5 polymorphs. These polyhedra are composed by corner- and edge-shared NbO_6 octahedra [33], structured with different extents of distortion since the corner-shared octahedra exhibit small distortions, while edge-shared octahedra undergo significant change in the Nb–O linkage distances, leading to larger distortions [33,34]. The H- Nb_2O_5 predominantly contain distorted NbO_6 and the tetrahedrally coordinated NbO_4 units structure is not a typical structure for Nb_2O_5

due to the large radii of Nb^{5+} ion to fit into an oxygen-anion tetrahedron [32], but also could exist into H-phase. Thus, the Raman spectrum for the niobium oxide precursor shows several bands centered at 265, 625, 670, 840 and 995 cm^{-1} , all assigned to Nb–O bonds contained different distorted NbO_6 octahedra. Bending modes of Nb–O–Nb linkages appear at low frequencies ($\sim 250\text{ cm}^{-1}$) and indicate clustering of NbO_n into the phosphate based chains [35].

Table 2 shows the Raman band assignments for the glass samples. The Raman bands of the glasses at 1150, 1013, 960 and 750 cm^{-1} are assigned to symmetric stretching vibration of Q^2 $(\text{PO}_3)^-$ chains, symmetric stretching of Q^1 $(\text{PO}_3)^{2-}$ groups, asymmetric stretching of Q^0 $(\text{PO}_4)^{3-}$ groups and P–O–P bonds, respectively [36]. Relatively weaker bands are observed as the relative amount of niobium oxide increases, indicating a modification in the phosphate network by intensity decrease phosphate assigned bands. Similar Raman evolution was observed for NaPO_3 – Nb_2O_5 binary glass system [37]. The addition of Nb_2O_5 gives rise a new, broad and intense band located initially at 845 cm^{-1} for P9N1 glass sample, which shifts to lower frequencies as Nb_2O_5 concentration increases, and located at 775 cm^{-1} for P4N6 glass sample. This band can be assigned to bending modes of Nb–O–Nb bonds in NbO_6 octahedral units and also terminal oxygen atoms of NbO_6 units, similar to the case for NaPO_3 – WO_3 glasses [38]. At this same region the coupled bending modes of Nb–O–P–Nb–O and symmetrical stretching vibrations of Nb–O bonds in NbO_6 octahedra units could also be observed [39]. However, due to the high concentration of niobium oxide this band was probably hindered by the highest intense band related to Nb–O–Nb modes [40]. The band shift observed from 845 cm^{-1} to 775 cm^{-1} is related to the increase of the neighborhood polarizability around the Nb–O⁻ terminal bonds and also because the decrease of Pb–O bonds concentration. This result corroborates the suggestion of

NbO₆ octahedra being progressively incorporated between phosphate tetrahedra units into the glass network, playing a role of glass former.

Table 2. Raman assignments for the niobium pyro-phosphate glasses (Raman shifts are in cm⁻¹).

Raman bands	Modes assignments	References
265	O – P – O and O – Nb – O coupled deformation modes	39
425	O – P – O and O – Nb – O coupled modes	39
620	Nb – O vibrations	39
750	Symmetric P – O – P bonds	36
775 - 845	Nb – O – Nb bending modes in NbO ₆	38, 39
960	Q ⁰ (PO ₄ ³⁻) asymmetric stretching vibrations	36
1013	Q ¹ (PO ₃ ²⁻) symmetric stretching vibrations	36
1150	Q ² (P – O – P) symmetric stretching vibrations	36

At lower frequency region, the Raman bands located at 265, 425 and 620 cm⁻¹ also increase in intensity as a function of Nb₂O₅ concentration and are respectively assigned to the deformation modes of Nb–O–Nb bridging bonds in NbO₆ octahedra, coupled modes of O–Nb–O and O–P–O bonds and vibrational modes of Nb–O bonds with Nb–O–Nb bridging, previously reported for α-NbPO₅ [39]. Also, it is an indicative of a three-dimensional niobium oxygen framework similar to those observed in LiNbO₃ and NaNbO₃ [41], where NbO₆ octahedra share corners, and only Nb–O–Nb bridging is present in these structures.

In general, Raman results combined with the thermal analysis depicts a structural evolution for the glass samples. It is possible to infer that Nb₂O₅ plays the role of glass former, in conjunction with the phosphate chains, up to 60 mol% of Nb₂O₅ (P6N4). The glass transition temperatures increase linearly with niobium oxide concentration, which is a strong indication that an increase of network connectivity happens. The addition of niobium oxide assists

promoting the increase of glass network connectivity with high three-dimensionality due to the formation of mixed structures composed by $(\text{O-P-O})_n\text{-Nb-O-Nb-}(\text{O-P-O})_m$ chains, by the replacement of phosphate tetrahedral coordinated groups, Q^n , by octahedral $[\text{NbO}_6]_n$ sharing common corners. At high Nb_2O_5 concentrations (above P6N4), a new network structure is formed constituted mainly by $[\text{NbO}_6]_n$ polyhedral, which reflect on the reduction of the glass thermal stability against crystallization and an enhancement of optical nonlinearity (nonlinear refractive index) due to the formation of niobium oxide polyhedral clusters. Similar behaviors were related by El Jazouli et al. in the ternary glass system $\text{Na}_2\text{O-P}_2\text{O}_5\text{-Nb}_2\text{O}_5$ [15].

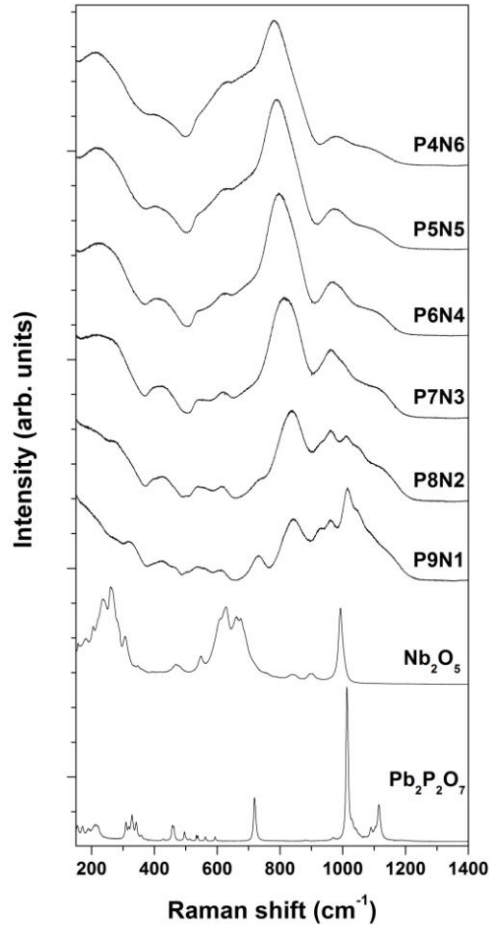


Figure 3. Raman spectra of raw materials and glasses samples produced in the binary system $\text{Pb}_2\text{P}_2\text{O}_7\text{-Nb}_2\text{O}_5$.

Linear and nonlinear optical properties

Figure 4 shows absorption spectra of the samples from 300 to 800 nm at room temperature. The increase of Nb₂O₅ concentration leads to a shift in the absorption edge to higher wavelengths, from ~ 370 nm for P9N1 to ~ 470 nm for P4N6, thus the incorporation of niobium oxide progressively decrease the bandgap energy as shown in Table 3. This behavior also can be related with the formation of more covalent network, as previously suggested by thermal analysis and Raman spectroscopy, attributed to the insertion of NbO₆ octahedra into the glass network among PO₄ units. The red shift in function of Nb₂O₅ is related to the reduced oxidation states of niobium ions. The colorless of P9N1 and P8N2 samples is related to the largest presence of Nb⁵⁺ species which contain d^0 electronic configuration. However, as the Nb₂O₅ concentration is increased above 30 mol %, the samples pass from yellow to dark yellow, probably due to the reduction of Nb⁵⁺ ions and formation of Nb⁴⁺ species, which has d^1 electronic configuration. Barbosa et al. [37] showed by electron paramagnetic resonance (EPR) analysis on the binary system NaPO₃–Nb₂O₅ glasses the presence of Nb⁴⁺ in samples containing more than 30 mol % of niobium oxide and melted at 1000 and 1400 °C, which also affect the Nb⁵⁺ ↔ Nb⁴⁺ equilibrium.

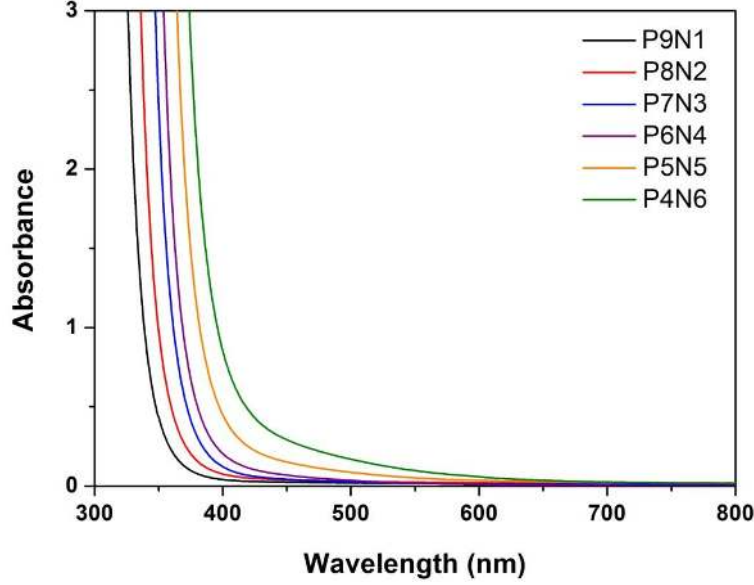


Figure 4. UV–Visible absorption spectra of the glasses samples in the binary system $\text{Pb}_2\text{P}_2\text{O}_7\text{--Nb}_2\text{O}_5$ with thickness of 2.10 ± 0.01 mm. Fresnel losses were corrected using reflectance measurements with a laser at 800 nm.

Generally, oxide glasses exhibit changes on optical edges according to the chemical nature of glass formers and modifiers and also is observed in transparent glass-ceramics [42,44]. For crystalline materials the optical absorption edge at ultraviolet or visible regions is directly related to the conduction and valence bands (direct and indirect transitions), whereas for non-crystalline materials the absorption spectrum shows a "tail broad" toward the high-energy side, shown in Figure 4. Glasses show an exponential increasing with the photon energy near the high-energy side (energy gap), such behavior is known as the Urbach edge and this dependence is given by using equation 3 [45]:

$$\alpha(h\nu) = \alpha_0 \exp\left(\frac{h\nu}{E_U}\right) \quad (\text{Eq. 3}),$$

where α_0 is a constant and E_U is the Urbach energy which is interpreted as the width of the valence band tails at localized states, associated with the structural disorder of amorphous state.

Then, direct and indirect optical band gap energy can be calculated via equation 4:

$$\alpha(h\nu) = A \frac{(h\nu - E_{opt})^p}{h\nu} \quad (\text{Eq. 4}),$$

where A is a constant called band tailing parameter, E_{opt} is the optical band gap, h is the Planck constant, and p is an index that depends on the nature of the electronic transitions responsible for the absorption ($p = 0.5$ for E_{dir} and $p = 2.0$ for E_{indir}) [46]. The optical band gap energy is also given in equation 4. E_{opt} were obtained by extrapolating the linear fitted regions to $(Ah\nu)^{1/2} = 0$, with a correlation coefficient of 0.995. The evaluation of optical absorption coefficient and the absorption edge values are important especially to connect with the theory of electronic structure for non-crystalline materials. The calculated optical band gaps (E_{dir} and E_{indir}) and Urbach energy E_U are plotted in Figure 5 as a function of Nb_2O_5 concentration. The increase of niobium oxide relative content results in a linear decrease of their E_{dir} and E_{indir} , and a linear increase of Urbach energy, E_U . The correlation coefficients were 0.998 and 0.996 for E_{dir} and E_{indir} , respectively. Such behavior observed in the direct, indirect and Urbach energies can be explained by the increase of network connectivity in the glass samples, which can be seen as a shift to longer wavelengths and a "tail broad" toward the high-energy side with increase of Nb_2O_5 concentration (Figure 5).

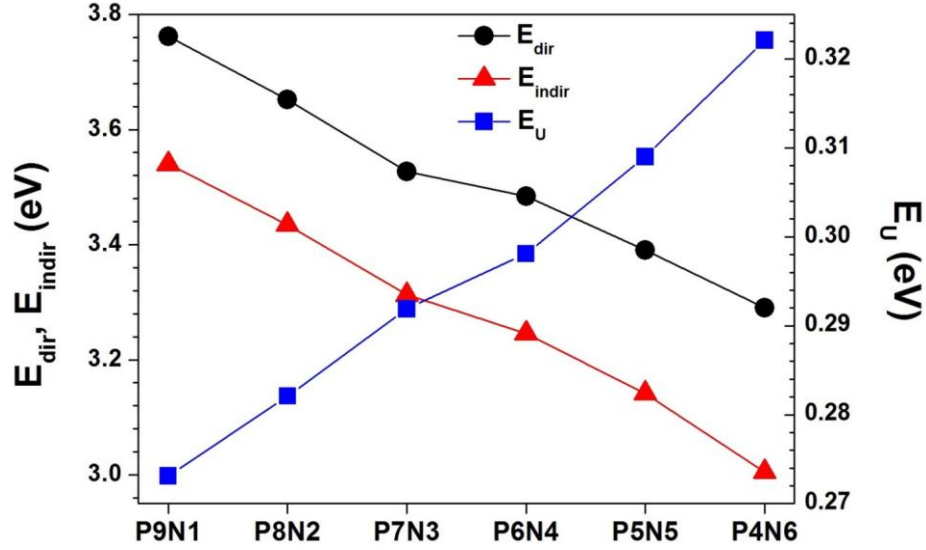


Figure 5. Optical band gap (E_{dir} and E_{indir}) and Urbach energy E_u (in eV) as a function of Nb_2O_5 molar concentration.

Figure 6(a) shows the refractive indexes and Figure 6(b) the dispersion curves of the linear refractive index as a function of Nb_2O_5 concentration. The measurements were performed at 538, 633 and 1550 nm in TE polarization. The increase of refractive index of 1.90 to 2.08 at 538 nm, 1.89 to 2.06 at 633 nm and 1.85 to 2.01 at 1550 nm can be understood by the high polarizability of niobium atoms due to their extended electron cloud owing to valence configuration d^0 and d^1 . In addition, as the refractive index depends on the electron density or ion polarizability, non-bridging oxygen (NBO) plays an important role to get larger values of refractive index. The number of NBO increases when the $Pb_2P_2O_7$ (glass former) is replaced by Nb_2O_5 due to the phosphate network break and formation of anionic oxygen, which also contribute to increase the refractive index as much NBO is formed [47]. This could also be related to the larger ionic radii of Pb^{2+} ions of 133 pm, compared with ionic radii of Nb^{+4} and Nb^{5+} ions of 68 and 64 pm, respectively. Thus, Nb–O bonds concentration are higher in comparison with P–O bonds per unit of volume [47,48], also leading to an increase of refractive index values. The high refraction

values obtained for PN glasses are unusual for phosphate-based glasses compositions and justify the exploration of nonlinear optical properties on that.

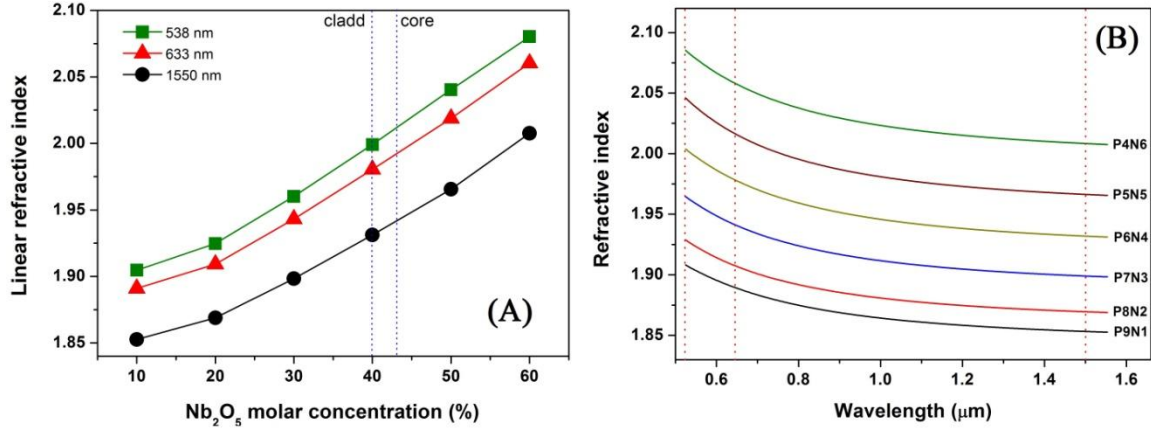


Figure 6. (a) Refractive indexes measured at 538, 633 and 1550 nm as a function of Nb_2O_5 content, and (b) the dispersion curves of the linear refractive index for the PN glasses.

From the optical band gap values (E_{opt}) we can evaluate the refractive indices (n_{opt}) in the optical absorption edge using equation 5 [49]:

$$\frac{n^2-1}{n^2+2} = 1 - \sqrt{\frac{E_{opt}}{20}} \quad (\text{Eq. 5}).$$

The refractive index values calculated are shown in Figure 7. The refractive index values quoted corresponds to the respective E_{opt} values (in nanometers) of the glass samples. Refractive index values increase almost linearly with the progressively replacement of $\text{Pb}_2\text{P}_2\text{O}_7$ by Nb_2O_5 in the glass system. The decrease in optical band gaps and increase of refractive index values are in agreement with the reported values by Honma et al. in 2002 and Dimitrov et al. in 2002 [50]. This decrease of E_{opt} may be due to the structural changes in function of Nb_2O_5 content. The increase of Nb_2O_5 may create states in the deep energy levels which causes the decrease of optical energy gap (Table 3).

Table 3. Cut-off wavelengths, optical band gap and Sellmeier coefficients calculated for the prepared glasses samples and optical fiber.

Samples	E _{opt} (eV)	b	c (nm ²)	d (x10 ⁻⁹)
P9N1	3.66	2.42	24048.52	2.83
P8N2	3.55	2.47	25362.38	1.33
P7N3	3.43	2.59	26806.87	4.68
P6N4	3.36	2.72	27523.81	7.39
P5N5	3.24	2.84	30563.40	2.95
P4N6	3.11	2.99	30695.78	4.48
Cladding	3.36	--	--	--
Core	3.32	--	--	--

The Sellmeier model is an empirical relationship between the refractive index and wavelength (λ) for a transparent medium, usually glass [51,52], and is only applicable to wavelength regions where absorption is negligible, as shown in equation 6 below:

$$n^2(\lambda) = 1 + \frac{b\lambda^2}{\lambda^2 - c} - d\lambda^2 \quad (\text{Eq. 6}),$$

where b, c, and d are determined experimentally from the absorption spectra and are used to characterize nonlinear optical devices, as detailed in [53]. Thus, to determine the minimum deviation between experimental and calculated values of refractive indices, an interactive process was used to find the Sellmeier's coefficients, which are summarized in Table 3. The correlation coefficient was 0.942±0.008. The parameters b and d are dimensionless coefficients, and represent the dispersion coefficients; c represents the effective resonance absorption wavelength in the ultraviolet region. The values of b and c increased with the increasing the Nb₂O₅

concentration (Table 3), i.e., the dispersion and absorption in these glasses increase as a function of Nb_2O_5 amount, as observed in Figures 4, 5, 6(b) and 7, while the values of d are in the same order of magnitude with a randomly behavior.

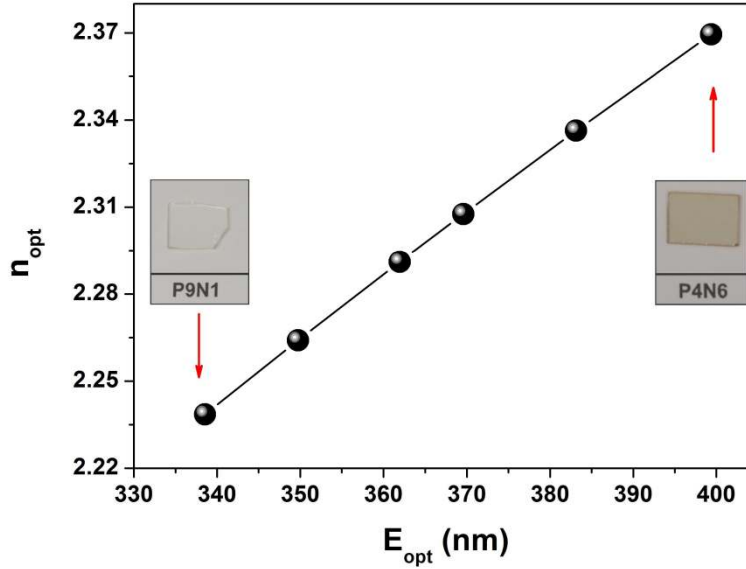


Figure 7. Refractive indices on each optical absorption edge.

Beside the linear optical properties we have also analyzed the influence of niobium addition on the third-order optical nonlinearities, represented by the nonlinear absorption and refraction. Figure 8 displays the spectra of two-photon absorption coefficient (β) for P9N1, P6N4 and N4N6 samples, along with typical open aperture Z-scan signature (inset). As one can note, the magnitude of β is improved according to the addition of niobium oxide, whereas it decreases when the excitation energy departs from the bandgap. At 500 nm, β values are 0.05 cm/GW, 0.30 cm/GW, and 0.39 cm/GW for P9N1, P6N4 and N4N6 samples, respectively. Such increase of β is related to the decrease of the optical bandgap energy, which favors the two-photon absorption process. Although the E_{opt} values obtained from the linear absorption (Table 3) would enable two-photon absorption up to 680 nm and 800 nm for the samples containing the lowest and

highest niobium concentration, it has been observed only in the spectral range reported in Figure 8 due to the low magnitude of two-photon absorption coefficient (β) at further wavelengths.

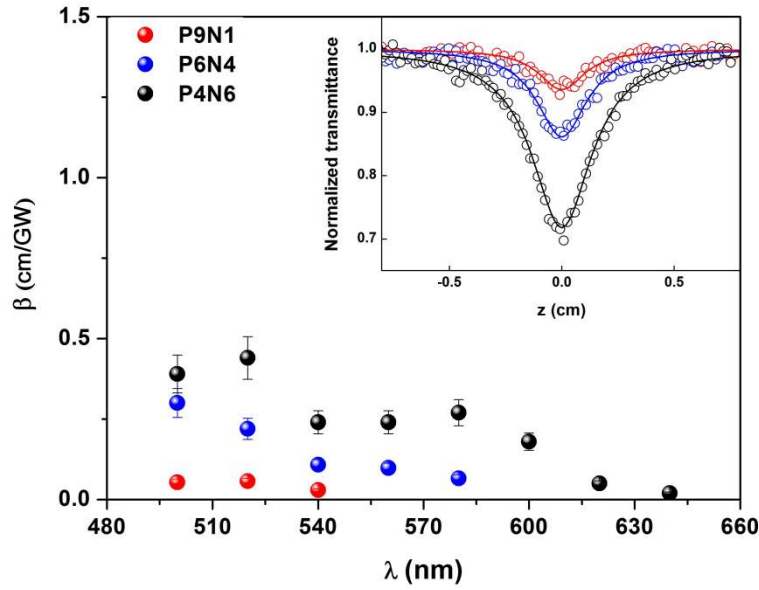


Figure 8. Two-photon absorption spectra of P9N1, P6N4 and P4N6 samples. The inset shows the closed aperture Z-scan signature for these samples at 540 nm, where symbols represent the experimental data and the continuous line is the fitting using equation 2.

Figure 9 displays the closed aperture z-scan signature at 620 nm of the samples P9N1 and P6N4, which contain the lowest and highest concentration of Nb_2O_5 , respectively. Symbols correspond to the experimental data, while the solid lines represent the model used to obtain the nonlinear index of refraction (n_2) [21]. The valley-peak configuration on the transmittance signal represents a positive n_2 , corresponding to an ultra-fast electronic effect of self-focusing. It is worth note that the effect of nonlinear absorption over refractive z-scan signatures has been deduced in the regions where two-photon absorption was detected.

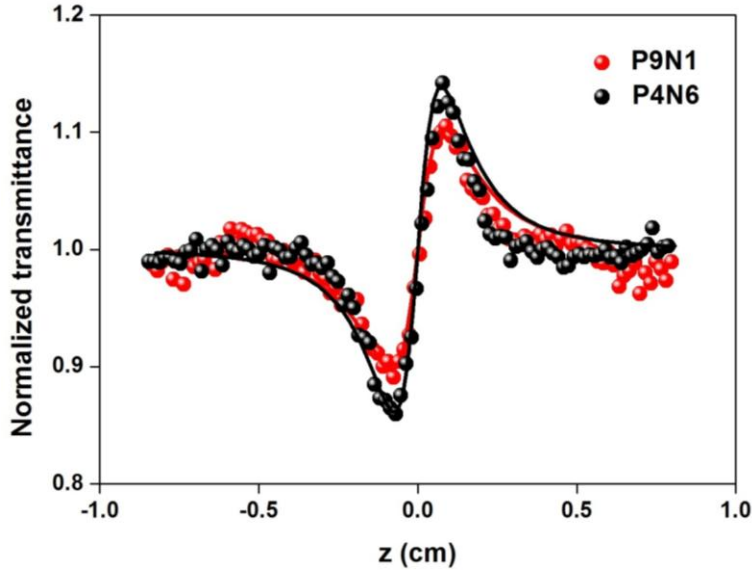


Figure 9. Closed aperture z-scan signature of P9N1 and P4N6 samples, containing respectively 10 and 60 %mol of Nb₂O₅, at 620 nm and femtosecond regime. Symbols represent the experimental data and the continuous line is the fitting using equation 1.

The n_2 spectra are shown in Figure 10, in which n_2 values can be considered constant from the visible to the telecom region, within the experimental error. No evidence of the resonance enhancement effect was observed when the excitation energy approaches to the band gap. Although such effect has been reported for bismuth-based glass [54], the absence of the n_2 enhancement in niobium-based glass might be associated with the low magnitude of the nonlinearities when compared with the former one, which has a nonlinear refraction at least two orders of magnitude higher. However, the n_2 mean value exhibited an increase with the Nb₂O₅ content, as seen on the inset of Figure 10. The average value of n_2 from 500-1500 nm is 2.2×10^{-19} , 2.8×10^{-19} and 3.8×10^{-19} m²/W for P9N1, P6N4 and P4N6 samples respectively, being 9 – 15 fold higher than fused silica [55]. Such behavior is in agreement with linear refractive data and it is based on structural changes caused by the Pb₂P₂O₇ replacement for Nb₂O₅. As a consequence of formation NbO₆ octahedra, there is an increase of terminal oxygen atoms, which

are responsible for improving the network polarizability without sacrificing its connectivity. In addition, the formation of Nb^{4+} rather than Nb^{5+} for samples with Nb_2O_5 content $\geq 30\%$ could further improve the optical nonlinearities due to extended electron cloud of d orbital [56]. The increase of the third-order susceptibility on account of niobium oxide addition has been reported not only in phosphate matrix, but also borate and silicate glasses [57]. Particularly in phosphate matrix, the clusterization of NbO_6 is assigned as the main responsible for the increase of the optical nonlinearities due to the formation of high-polarizable Nb-O-Nb bounds [58].

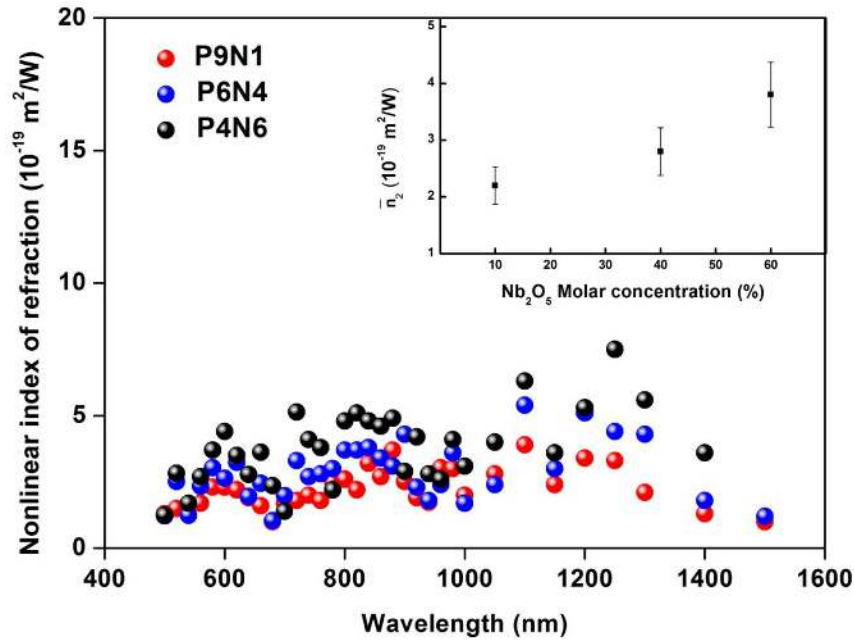


Figure 10. Spectra of the nonlinear index of refraction of P9N1, P6N4 and P4N6 samples obtained by z-scan technique. The inset shows the dependence of n_2 (average values from 500-1500 nm) with Nb_2O_5 concentration. Experimental error of n_2 values is around 15%.

Niobium lead-pyrophosphate step index optical fiber

In order to check the reproducibility and to optimize the process for step-index preform fabrication from $\text{Pb}_2\text{P}_2\text{O}_7\text{-Nb}_2\text{O}_5$ binary glass system, a chromium doped preform with 0.5 mol % of Cr_2O_3 was previously produced using different piston downward speeds. The color in the

core is due to the *d-d* electron transitions of Cr^{3+} ions (tracer ion) and was used to measure and monitor the core diameter, core centricity and also the uniformity of core-cladding interface along the preforms lengths. The preform monitoring was accomplished by slicing the preforms into cross-sections which were optically polished and inspected using a Nikon D7100 DSLR camera. Approximately 12 slices with a thickness of ~ 3 mm were obtained from each preform, which had an outer diameter of 10.11 mm. The preform obtained by using the slower piston speed of 240 mm/min presented the smaller core diameter of 4.5 ± 0.3 mm, and was used to produce the optical fiber.

For the production of preforms and optical fibers to be applied in nonlinear optics and photonics, the glass composition was chosen considering two important parameters: (i) the highest refractive index, and (ii) the highest thermal stability against crystallization. It is worth mentioning that good thermo-mechanical resistance is also desirable for optical fiber, but this parameter was not evaluated in this work. However, the optical fiber produced has good mechanical resistance and can be handling and packaging without polymeric coating under atmospheric environment. Thus, the chosen composition was the P6N4 glass sample, although it has not the highest linear refractive index, this sample present the higher thermal stability parameter of $\Delta T = 252$ °C, stable enough to perform the drawing process. The drawing temperature for the chosen composition was found to be 715 °C and more than 100 meters of fiber were obtained free of crystallization and color changes. In order to ensure that the drawing conditions not induced nucleation or crystallization, the temperature of the tower furnace (hot zone and pre-heat zone) was mapped and the time in this zone was controlled during the drawing process, which was kept under nitrogen atmosphere. Indeed, as the fiber drawing process is performed above T_g , the larger is the ΔT values, the lower is the crystallization tendency during

the drawing process, since the presence of crystals within an optical fiber dramatically reduces its optical and mechanical properties [28,29].

The optical micrograph in Figure 11 shows the cross-section of the fabricated fiber, presenting good core circularity/concentricity. It shows the fiber has a total diameter of 234 μm and its core has a diameter of 117 μm . A multi-mode step index optical fiber was obtained and there is no apparent delimitation, crack or bubbles at their interface, which is an important aspect for enabling light propagation into the core.

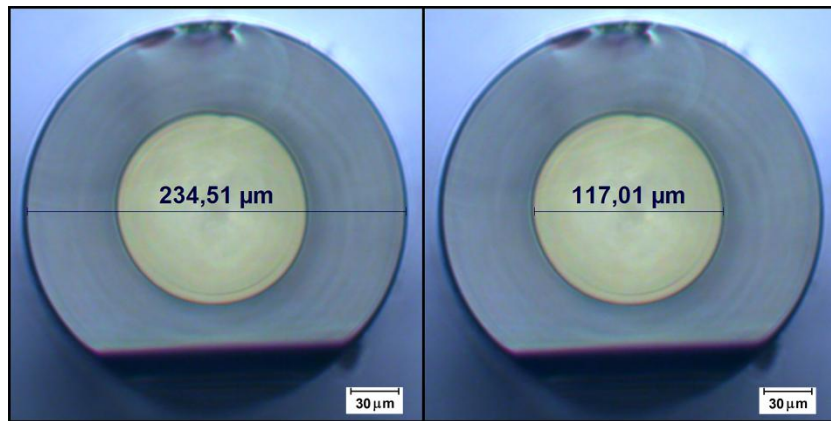


Figure 11. Cross-section view of the PN step-index optical fiber observed with an optical microscope.

As indicated by vertical dotted line in Figure 6(a), the refractive index difference between core (P5.7N4.3) and cladding (P6N4) is 0.02 at 633 nm, which corresponds to a numerical aperture of 0.25. This index profile difference is sufficiently to have optical confinement inside the core of the fiber [59]. In order to achieve a large numerical aperture (NA), a large difference of refractive indices between core and cladding must be arranged. Nevertheless, the range of indices available for transparent glasses is relatively small and depends on the chemical composition of the glass host. For the niobium pyro-phosphate optical fiber produced in this

work, the NA calculated by using the follow equation are 0.2239, 0.2165 and 0.2026 at 538, 633 and 1550 nm, respectively.

$$NA = \sqrt{n_{core}^2 - n_{cladding}^2} \quad (\text{Eq. 7})$$

The propagation losses of the PN step index fiber were measured at 632.8 nm and with a white light source by the cut-back method. For cut-back measurement a He-Ne laser was couple into a 30 cm of fiber using a 40x microscope objective. The propagation losses equal to (35±0.4) dB/m has been obtained. Measurements carried out using white light showed a decrease of the propagation loss with the increase of the wavelength, being (20±0.6) dB/m at 900 nm. The high optical losses obtained are due to the presence of impurities, such as transition metals and OH groups inside the glasses, since the suction method allows the production of preforms with good quality interface between core and cladding compositions.

4. Conclusions

The synthesis and characterization of a new stable binary glass system based on $\text{Pb}_2\text{P}_2\text{O}_7$ – Nb_2O_5 was presented. Up to 60 mol % of Nb_2O_5 were added to the sample, obtaining glasses with good thermal stability and high glass transition temperatures associated with structural changes induced by Nb_2O_5 addition. As a result of this incorporation, the glassy samples showed high refractive index values, making these materials good candidates for nonlinear optical applications, as well as luminescent hosts when doped with rare earth ions. In fact, the nonlinear index of refraction is one order of magnitude higher than fused silica. Although no significant change was observed in each particular n_2 spectrum (500-1500 nm), there is an increase on the average n_2 values from 2.2×10^{-19} to $3.8 \times 10^{-19} \text{ m}^2/\text{W}$ when the amount of Nb_2O_5 was raised from 10 to 60 mol%. Such increase on the optical nonlinearity follows the increase of the linear

refractive index and can be explained by the structural changes, in which the formation of $[\text{NbO}_6]_n$ polyhedral favors the polarizability of the matrix. In addition, we also report the production of core-cladding preforms and optical fibers from the studied composition, with multimode step index profile by using the suction method. The method was effective to obtain preform with good core centricity, without cracks and bubbles, and very good core-cladding interface, reinforcing the efficiency of the suction method to obtain step index preforms. The new optical fiber obtained also showed good core centricity, absence of bubble and cracks, which can cause more light scattering that reduces the guiding efficiency of the fiber. In general, the glasses and optical fibers reported in this work showed enough optical properties for applications in nonlinear optical devices, such as the potentiality to generate supercontinuum spectrum under femtosecond excitation regime. For our best knowledge, this is the first time it is reported the production of optical fibers based on $\text{Pb}_2\text{P}_2\text{O}_7\text{--Nb}_2\text{O}_5$ glass system. Future research consist on to design, fabricate and characterize passive and lanthanide doped optical fibers, as well as the improvement of the preform fabrication methods to produce single-mode and microstructured optical fibers for nonlinear photonics applications.

Acknowledgements

The authors acknowledge, grants numbers 2010/20776-5, 2013/07793-6, 2011/12399-0 and 2011/21434-3 from São Paulo Research Foundation – FAPESP, Air Force Office of Scientific Research (FA9550-12-1-0028), CAPES, and CNPq (502391/2014-6) for financial support.

References

1. D. Manzani, R. G. Fernandes, Y. Messaddeq, S. J. L. Ribeiro, F. C. Cassanjes, G. Poirier, Thermal, structural and optical properties of new tungsten lead-pyrophosphate glasses, *Opt. Mater.* 33 (2011) 1862-1866.
2. T. R. Oliveira, K. Fedus, D. Manzani, E. L. Falcão-Filho, G. Boudebs, C. B. de Araújo, Y. Messaddeq, Near-infrared Kerr nonlinearity of $\text{Pb}(\text{PO}_3)_2\text{-WO}_3$ glasses, *J. Appl. Phys.* 108 (2010) 103523.
3. R. K. Brow, Review: the structure of simple phosphate glasses, *J. Non-Cryst. Solids* 263 (2000) 1-28.
4. J. H. Campbell, T. I. Suratwala, Nd-doped phosphate glasses for high-energy/high-peak-power lasers, *J. Non-Cryst. Solids* 263 (2000) 318-341.
5. G. Poirier, A. Michalowicz, Y. Messaddeq, S. J. L. Ribeiro, Local order around tungsten atoms in tungstate fluorophosphates glasses by X-ray absorption spectroscopy, *J. Non-Cryst. Solids* 351 (2005) 3644-3648.
6. E. Fargin, A. Berthereau, T. Cardinal, G. Le Flem, L. Ducasse, L. Canioni, P. Segonds, L. Sarger, A. Ducasse, Optical non-linearity in oxide glasses, *J. Non-Cryst. Solids* 203 (1996) 96-101.
7. T. Cardinal, E. Fargin, G. Le Flem, M. Couzi, L. Canioni, P. Segonds, L. Sarger, A. Ducasse, F. Adamietz, Nonlinear optical properties of some niobium (V) oxide glasses, *Eur. J. Solid State Inorg. Chem.* 33 (1996) 597.
8. D. Manzani, J. M. P. Almeida, M. Napoli, L. De Boni, M. Nalin, C. R. M. Afonso, C. Mendonça, S.J.L. Ribeiro, Nonlinear Optical Properties of Tungsten Lead-Pyrophosphate Glasses Containing Metallic Copper Nanoparticles, *Plasmonics* 8 (2013) 1667-1674.

9. E.L. Falcão-Filho, C. A. C. Bosco, G. S. Maciel, C. B. de Araújo, L. H. Acioli, M. Nalin, Y. Messaddeq, Ultrafast nonlinearity of antimony polyphosphate glasses, *Appl. Phys. Lett*, 83 (2003) 1292-1295.]
10. S. F. Khor, Z. A. Talib, W. M. Mat Yunus, Optical properties of ternary zinc magnesium phosphate glasses, *Ceram. Int.* 38 (2012) 935-940.
11. M. Yamane, Y. Asahara, *Glasses for Photonics*, first edition, Cambridge University Press, Cambridge-UK, 2000.
12. Y. M. Moustafa, K. El-Egili, Infrared Spectra of Sodium Phosphate Glasses, *J. Non-Cryst. Solids* 240 (1998) 144-153.
13. A. Langar, C. Bouzidi, H. Elhouichet, M. Férid, Er-Yb codoped phosphate glasses with improved gain characteristics for an efficient 1.55 μ m broadband optical amplifiers, *J. Lumin.* 148 (2014) 249-255.
14. D. Manzani, C. B. de Araujo, G. Boudebs, Y. Messaddeq, S. J. L. Ribeiro, The role of Bi_2O_3 on the thermal, structural, and optical properties of tungsten-phosphate glasses, *J. Phys. Chem. B* 117 (2013) 408–414.
15. A. El Jazouli, J. C. Viala, C. Parent, G. Le Flem, P. Hagenmuller, Structural investigation of glasses belonging to the $\text{Na}_2\text{O-Nb}_2\text{O}_5\text{-P}_2\text{O}_5$ system, *J. Solid State Chem.* 73 (1988) 433-439.
16. W. S. Key, J.C. Miller, Phosphate glass for photonics, *ORNL Rev.*, 27 (1994) 12-15.
17. R. Pyare, L.J. Lal, V.C. Joshi, V.K. Singh, Leachability of molybdenum from ternary phosphate glasses, *J. Am. Ceram. Soc.* 79 (1996) 1329-1334.

18. A. H. Khafagy, S. M. ElpRabaie, A. A. Higazy, A. S. Eid, Absorption spectra of zinc-phosphate glasses doped with Nd_2O_3 rare earth oxide, *Indian J. Phys.* 72(A) (2000) 433-439.
19. Z. Teixeira, O. Alves, I. Mazali, Structure, thermal behavior, chemical durability, and optical properties of the $\text{Na}_2\text{O}-\text{Al}_2\text{O}_3-\text{TiO}_2-\text{Nb}_2\text{O}_5-\text{P}_2\text{O}_5$ glass system, *J. Am. Ceram. Soc.* 90(1) (2007) 256–263.
20. D. Manzani, Y. Ledemi, I. Skripachev, Y. Messaddeq, S. J. L. Ribeiro, R. E. P. de Oliveira, C. J. S. de Matos, Yb^{3+} , Tm^{3+} and Ho^{3+} triply-doped tellurite core-cladding optical fiber for white light generation, *Opt. Mater. Express* 1 (2011) 1515–1526.
21. M. Sheikbahae, A. A. Said, E. W. Vanstryland, High-sensitivity single-beam n_2 measurements, *Opt. Letters* 14 (1989) 955-957.
22. M. Sheikbahae, A. A. Said, T. H. Wei, D. J. Hagan, and E. W. van Stryland, Sensitive Measurement of Optical Nonlinearities Using a Single Beam. *Ieee Journal of Quantum Electronics*. 26 (1990) 760-769.
23. J. M. P. Almeida, L. De Boni, A. C. Hernandes, C. R. Mendonca, Third-order nonlinear spectra and optical limiting of lead oxifluoroborate glasses, *Opt. Express* 19 (2011) 17220-17225.
24. J. G. Titchmarsh, US Pat., 4 217 123, 1978.
25. N. S. Prasad, J. Wang, R. K. Pattnaik, H. Jain, J. Toulouse, Preform fabrication and drawing of KNbO_3 modified tellurite glass fibers, *J. Non-Cryst. Solids* 352 (2006) 519-523.
26. D. C. Tran, C. F. Fischer, G. H. Sigel, Fluoride glass preforms prepared by a rotational casting process, *Elect. Let.* 18 (1982) 657-658.

27. K. Clarke, Y. Ito, Manufacture of fluoride glass preforms, *J. Non-Cryst. Solids* 140 (1992) 265–268.
28. A. Lin, A. Zhang, E. J. Bushong, J. Toulouse, Solid-core tellurite glass fiber for infrared and nonlinear applications, *Opt. Express* 17(19) (2009) 16716-16721.
29. V. A. G. Rivera, M. El-Amraoui, Y. Ledemi, Y. Messaddeq, E. Marega Jr., Expanding broadband emission in the near-IR via energy transfer between Er^{3+} - Yb^{3+} co-doped tellurite-glasses, *J. Lumin.* 145 (2014) 787–792.
30. T. Ikeya, M. Senna, Change in the structure of niobium pentoxide due to mechanical and thermal treatments, *J. Non-Cryst. Solids* 105 (1988) 243-250.
31. J. G. Weissman, E. I. Ko, P. Wynblatt, J. M. Howe, High-resolution electron microscopy and image simulation of TT-, T-, and H-niobia and model silica-supported niobium surface oxides, *Chem. Mater.* 1 (1989) 187-193.
32. Jih-Mirn Jehng, I.E. Wachs, Structural chemistry and Raman spectra of niobium oxides, *Chem. Mater.* 3(1) (1991) 100-107.
33. A. A. McConnell, J. S. Aderson, C. N. R. Rao, Raman spectra of niobium oxides, *Spectrochim. Acta Part A Mol. Spectrosc.* 32 (1976) 1067-1076.
34. B. M. Gatehouse, A. Wadsley, The crystal structure of the high temperature form of niobium pentoxide, *Acta Crystallogr.* 17 (1964) 1545-1554.
35. B. Orel, M. Macek, J. Grdadolnik, A. Meden, In situ UV-Vis and ex situ IR spectroelectrochemical investigations of amorphous and crystalline electrochromic Nb_2O_5 films in charged/discharged states, *J. Solid State Electrochem.* 2 (1998) 221-236.

36. I. W. Donald, Preparation, properties and chemistry of glass- and glass-ceramic-to-metal seals and coatings, *J. Mater. Sci.* 28 (1993) 2841-2886.
37. A. J. Barbosa, F. A. Dias Filho, L. J. Q. Maia, Y. Messaddeq, S. J. L. Ribeiro, R. R. Gonçalves, Er^{3+} doped phosphoniobate glasses and planar waveguides, structural and optical properties, *J. Phys.: Condens. Matter* 20 (2008) 285224.
38. C. C. Araujo, W. Strojek, L. Zhang, H. Eckert, G. Poirier, S. J. L. Ribeiro, Y. Messaddeq, Structural studies of $\text{NaPO}_3\text{-WO}_3$ glasses by solid state NMR and Raman spectroscopy, *J. Mater. Chem.* 16 (2006) 3277-3284.
39. A. El Jazouli, R. Brochu, J. C. Viala, R. Ohazcuaga, C. Delmas, G. Le Flem, *Ann. Chim. Fr.* 7 (1982) 285-291.
40. T. Cardinal, E. Fargin, G. Le Flem, S. Leboiteux, Correlations between structural properties of $\text{Nb}_2\text{O}_5\text{-NaPO}_3\text{-Na}_2\text{B}_4\text{O}_7$ glasses and non-linear optical activities, *J. Non-Cryst. Solids* 222 (1997) 228-234.
41. Y. D. Juang, S. B. Dai, Y. C. Wang, W. Y. Chou, J. S. Hwang, M. L. Hu, W. S. Tse, Phase transition of $\text{Li}_x\text{Na}_{1-x}\text{NbO}_3$ studied by Raman scattering method, *Solid State Commun.* 111 (1999) 723-728.
42. S. Sindhu, S. Sanghi, A. Agarwal, V. Seth, N. Kishore, Effect of BiO content on the optical band gap, density and electrical conductivity of $\text{MO}\cdot\text{BiO}\cdot\text{BO}$ ($\text{M}=\text{Ba}, \text{Sr}$) glasses, *Mater. Chem. Phys.* 90 (2005) 83-89.
43. D. Arsova, Bond arrangement and optical band gap in $\text{Ge}_x\text{As}_{40-x}\text{S}(\text{Se})_{60}$ glasses and thin films, *J. Phys. Chem. Solids* 57(9) (1996) 1279-1283.
44. Y. Ledemi, A-A. Trudel, V. A. G. Rivera, S. Chenu, E. Véron, L. A. Nunes, M. Allix, Y. Messaddeq, White light and multicolor emission tuning in triply doped

- Yb³⁺/Tm³⁺/Er³⁺ novel fluoro-phosphate transparent glass-ceramics, *J. Mat. Chem. C.* 2 (2014) 5046-5056.
45. X. Qiao, X. Fan, M. Wang, J.-L. Adam, X. Zhang, Spectroscopic properties of Er³⁺/Yb³⁺ co-doped 50SiO₂-20Al₂O₃-30CaF₂ glass and glass ceramics, *J. Phys.: Condens. Matter.* 18 (2006) 6937-6942.
 46. E. A. Davis, N. F. Mott, Conduction in non-crystalline systems V. Conductivity, optical absorption and photoconductivity in amorphous semiconductors, *Philos. Mag.* 22 (1970) 903–922.
 47. S. Hocde, S. Jiang, X. Peng, N. Peyghambarian, T. Luo, M. Morrell, Er³⁺ doped boro-tellurite glasses for 1.5 μ m broadband amplification, *Opt. Mater.* 25 (2004) 149–156.
 48. W. D. Kingery, H. K. Bowen, D. R. Uhlmann, *Introduction to Ceramics*, fourth edition, Wiley, New York, 1976.
 49. V. Dimitrov, S. Sakka, Electronic oxide polarizability and optical basicity of simple oxides, *J. Appl. Phys.* 79(3) (1996) 1736-1740.
 50. V. Dimitrov, T. Komatsu, Interionic interactions, electronic polarizability and optical basicity of oxide glasses, *J. Ceram. Soc. Jpn*, 108 (2010) 330-338.
 51. W. Sellmeier, Zur Erklärung der abnormen Farbenfolge im Spectrum einiger Substanzen, *Ann. Phys. Chem.* 143 (1871) 271.
 52. V. A. G. Rivera, Y. Ledemi, S. P. A. Osorio, D. Manzani, F. A. Ferri, S. J. L. Ribeiro, L. A. O. Nunes, E. Marega Jr., Tunable plasmon resonance modes on gold nanoparticles in Er³⁺-doped germanium tellurite glass, *J. Non-Cryst. Solids* 378 (2013) 126-134.

53. G. Ghosh, Sellmeier coefficients for the birefringence and refractive indices of ZnGeP_2 nonlinear crystal at different temperatures, *Appl. Opt.*, 37(7) (1998) 1205.
54. Z-scan study of third-order optical nonlinearities in bismuth-based glasses, T. Hasegawa, T. Nagashima, N. Sugimoto, *Optics Communications* 250 (2005) 411-415.
55. D. Milam, Review and assessment of measured values of the nonlinear refractive-index coefficient of fused silica, *Appl. Opt.*, 37 (1998) 546-550.
56. G. Boudebs, K. Fedus, Absolute measurement of the nonlinear refractive indices of reference materials, *J. Appl. Phys.* 105 (2009) 103106.
57. S. Santran, L. Canioni, T. Cardinal, E. Fargin, G. Le Flem, C. Rouyer, Precise and absolute measurements of the complex third-order optical susceptibility, *J. Opt. Soc. Am. B* 21 (2004) 349-359.
58. A. Flambard, J. J. Videau, L. Delevove, T. Cardinal, C. Labrugère, C.A. Rivero, M. Couzi, L. Montagne, Structure and nonlinear optical properties of sodium-niobium phosphate glasses, *J. Non-Cryst. Solids* 354 (2008) 3540-3547.
59. M. Boivin, M. El-Amraoui, Y. Ledemi, S. Morency, R. Vallée, Y. Messaddeq, Germanate-tellurite composite fibers with a high-contrast step-index design for nonlinear applications, *Opt. Mat. Express* 4 (2014) 1740-1746.

Table 1. Molar composition of the glassy samples and their characteristic temperatures.

Sample label	Pb ₂ P ₂ O ₇ (mol%)	Nb ₂ O ₅ (mol%)	T _g (°C)	T _x (°C)
P9N1	90	10	427 ± 2	524
P8N2	80	20	467 ± 2	598
P7N3	70	30	526 ± 2	704
P6N4	60	40	555 ± 2	807
P5N5	50	50	568 ± 2	756
P4N6	40	60	592 ± 2	700
Core	60	40	555 ± 2	807
Cladding	57	43	559 ± 2	803

Table 2. Raman assignments for the niobium pyro-phosphate glasses (Raman shifts are in cm^{-1}).

Raman bands	Modes assignments	References
265	O – P – O and O – Nb – O coupled deformation modes	39
425	O – P – O and O – Nb – O coupled modes	39
620	Nb – O vibrations	39
750	Symmetric P – O – P bonds	36
775 - 845	Nb – O – Nb bending modes in NbO_6	38, 39
960	$\text{Q}^0 (\text{PO}_4^{3-})$ asymmetric stretching vibrations	36
1013	$\text{Q}^1 (\text{PO}_3^{2-})$ symmetric stretching vibrations	36
1150	$\text{Q}^2 (\text{P} - \text{O} - \text{P})$ symmetric stretching vibrations	36

Table 3. Cut-off wavelengths, optical band gap and Sellmeier coefficients calculated for the prepared glasses samples and optical fiber.

Samples	E_{opt} (eV)	b	c (nm²)	d (x10⁻⁹)
P9N1	3.66	2.42	24048.52	2.83
P8N2	3.55	2.47	25362.38	1.33
P7N3	3.43	2.59	26806.87	4.68
P6N4	3.36	2.72	27523.81	7.39
P5N5	3.24	2.84	30563.40	2.95
P4N6	3.11	2.99	30695.78	4.48
Cladding	3.36	--	--	--
Core	3.32	--	--	--

Figure 1

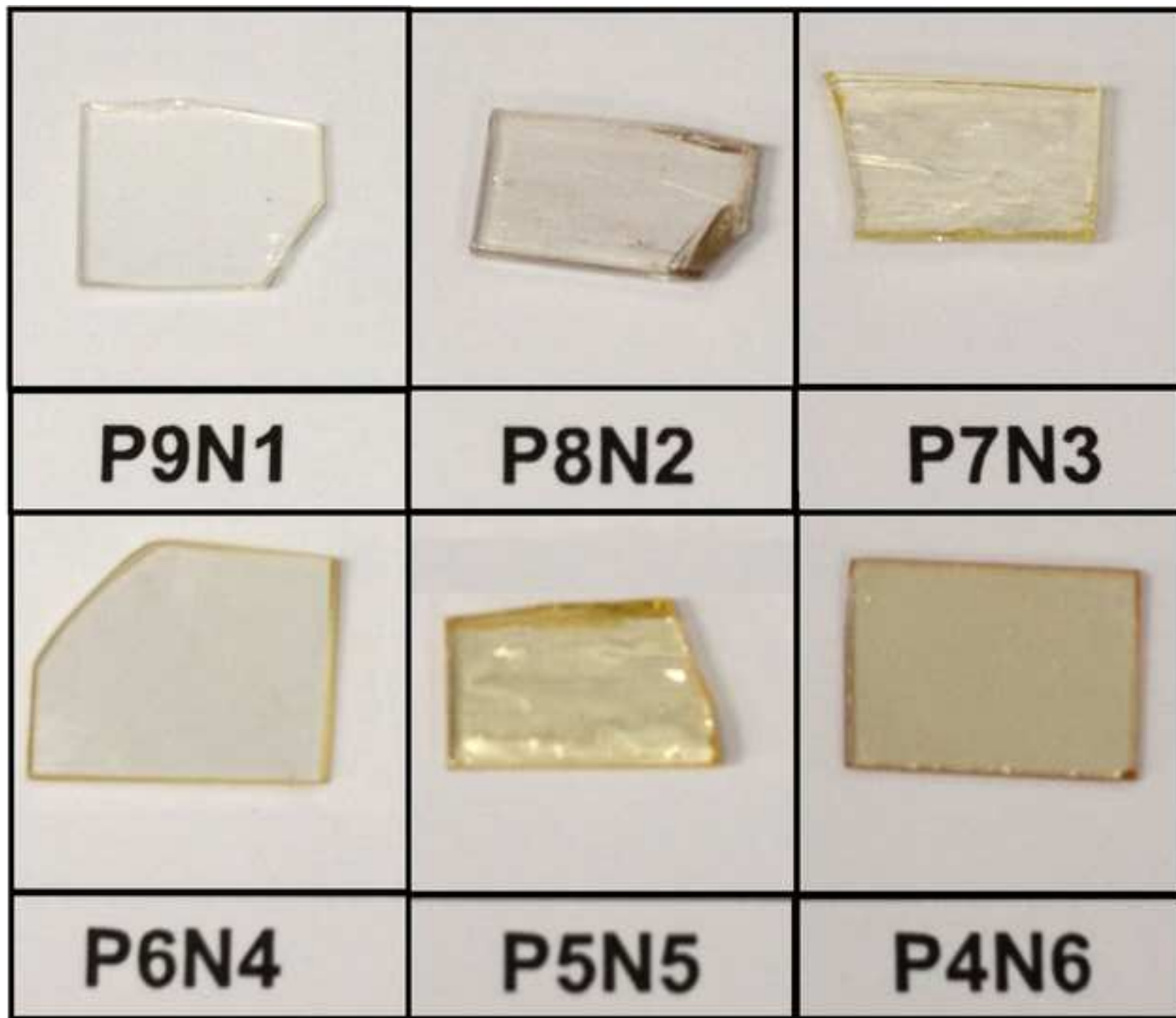


Figure 2

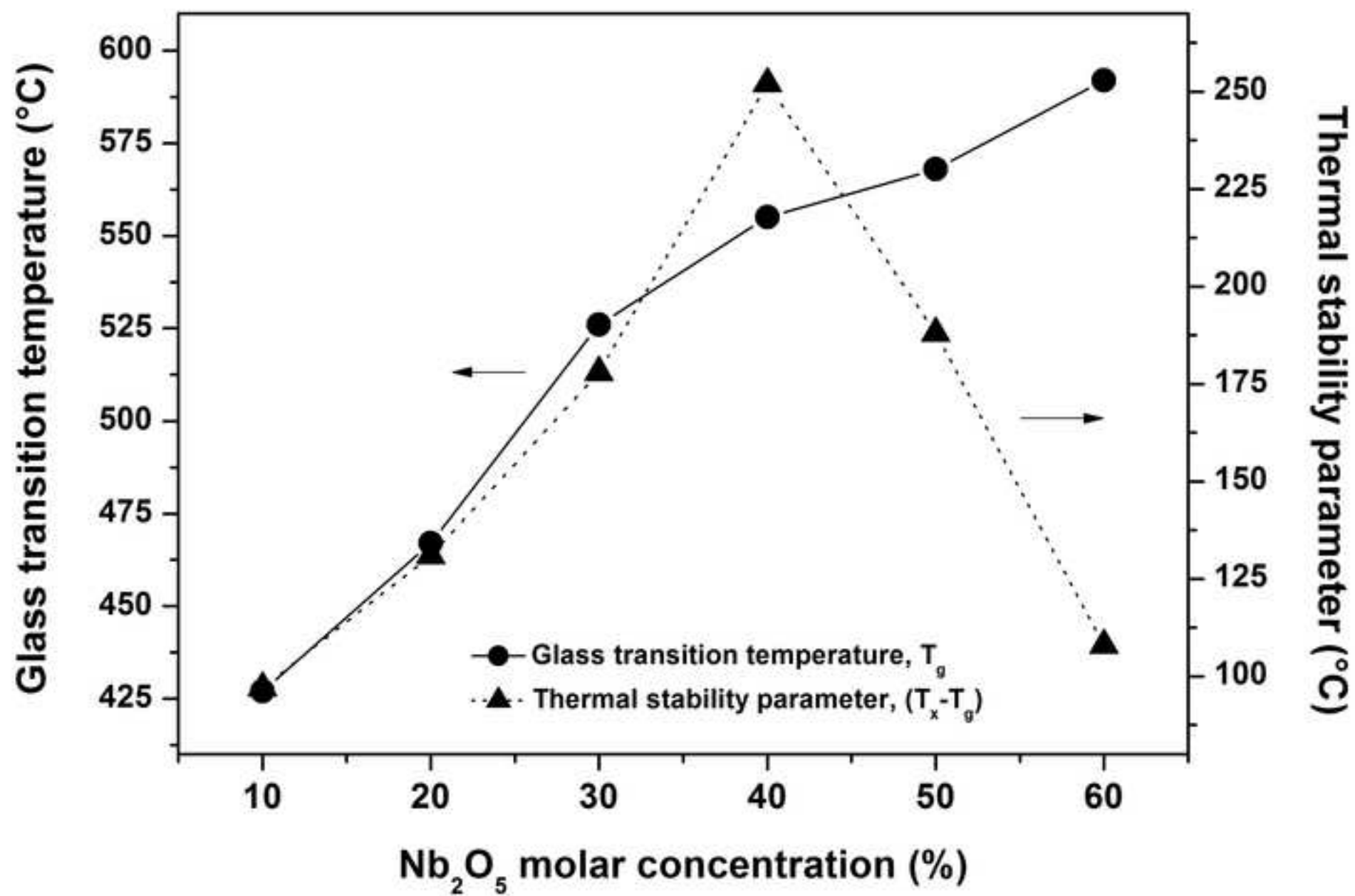


Figure 3

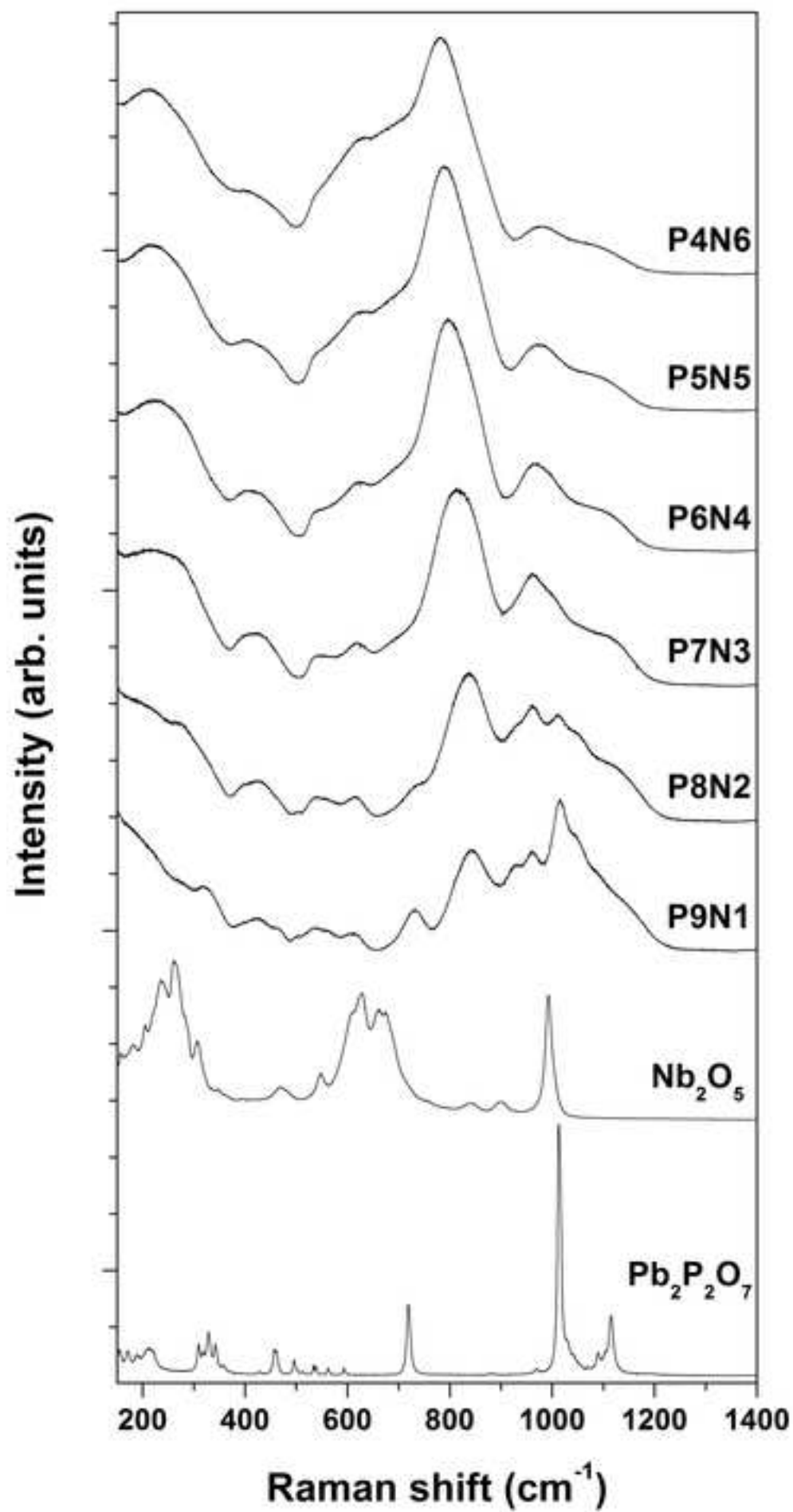


Figure 4

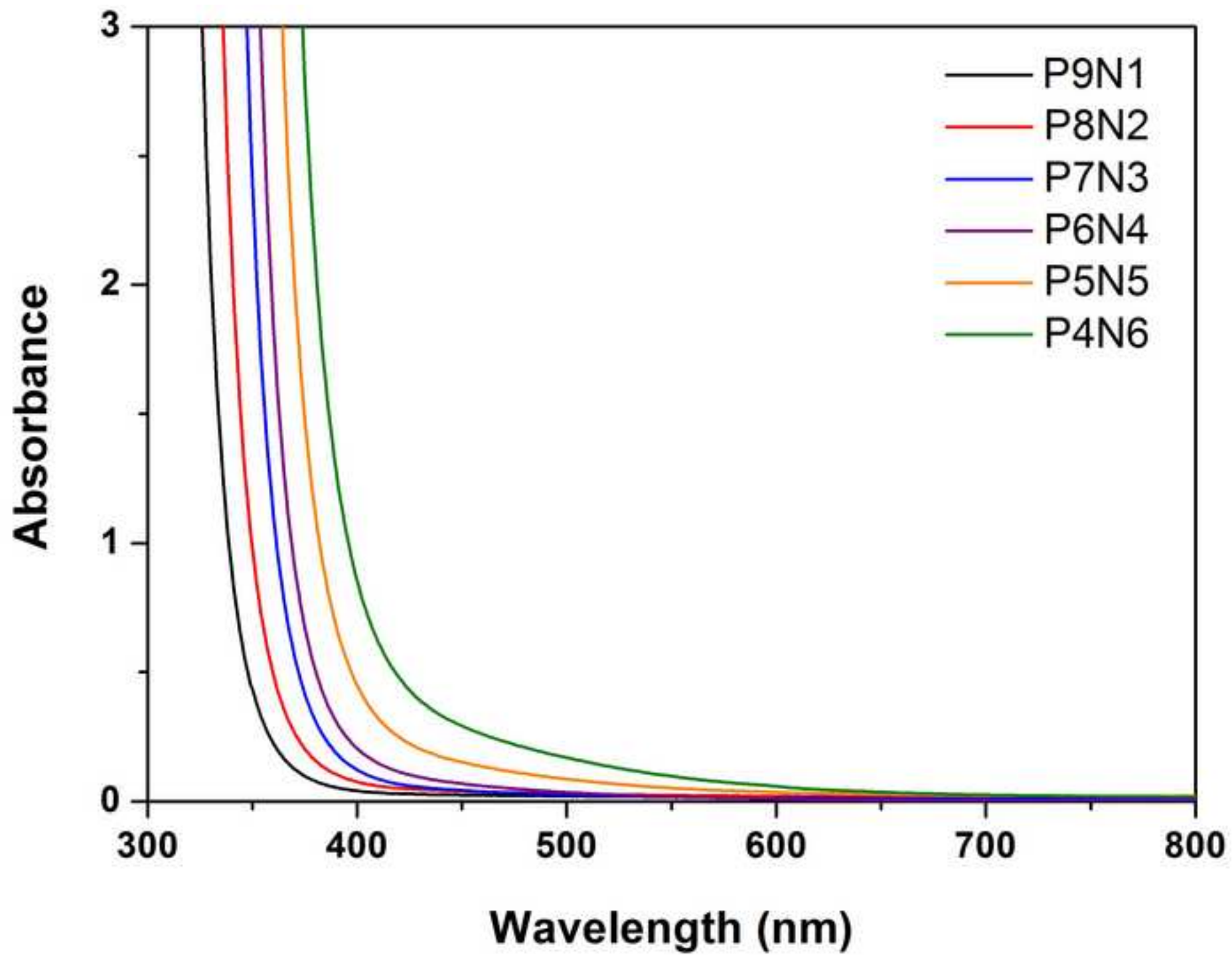


Figure 5

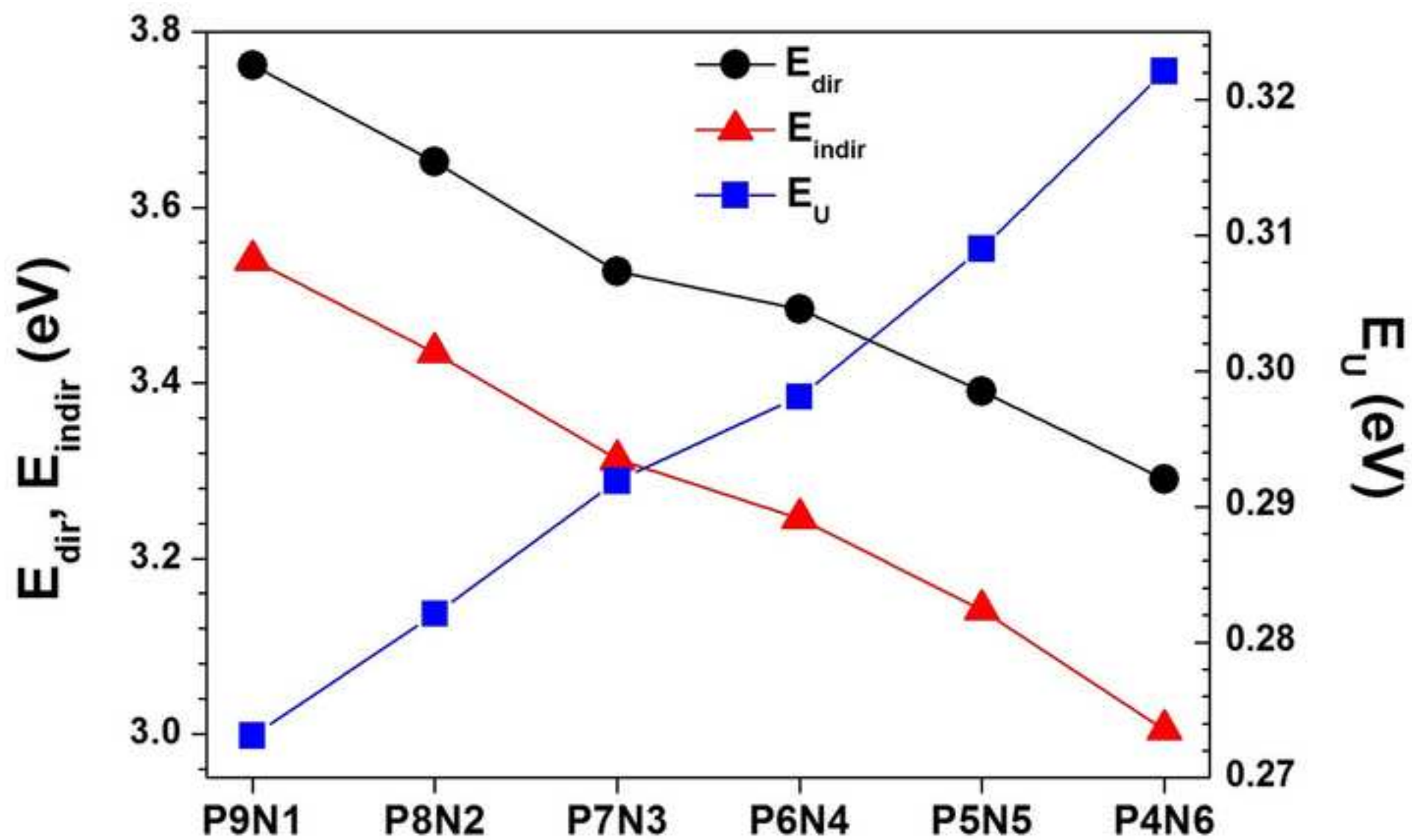


Figure 6

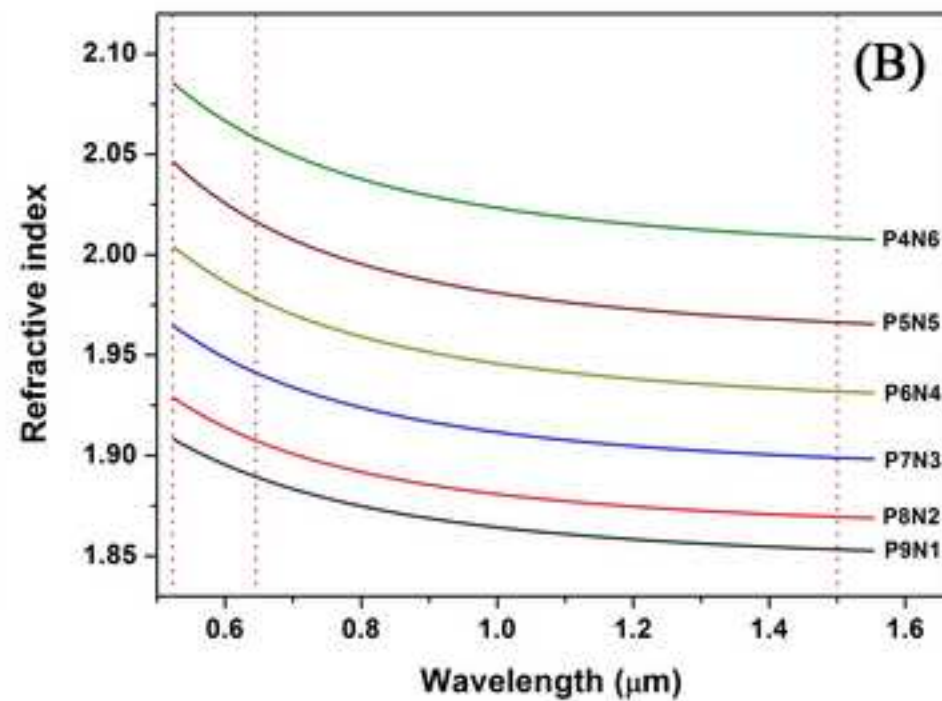
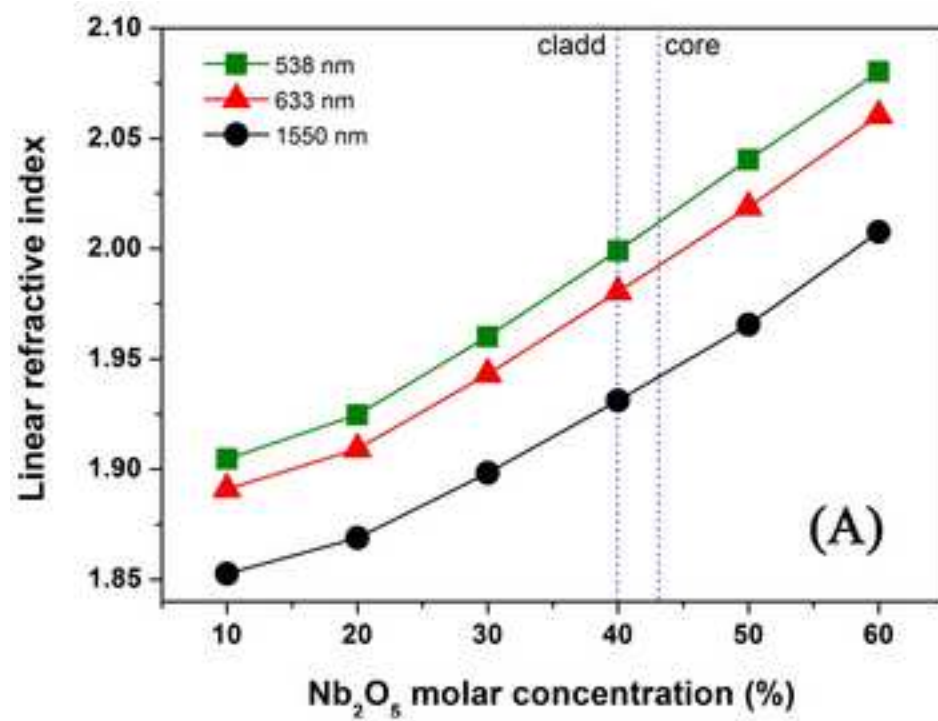


Figure 7

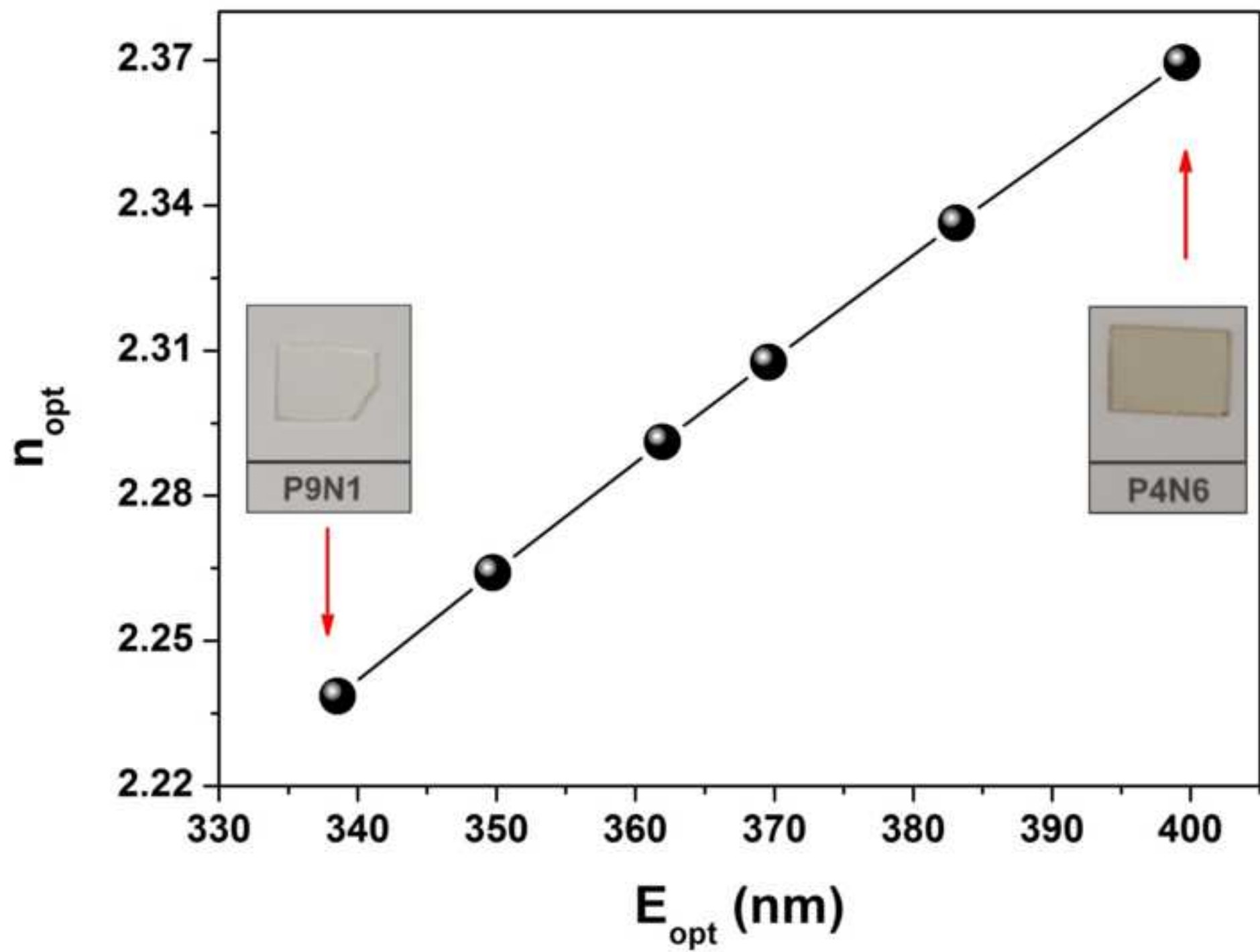


Figure 8

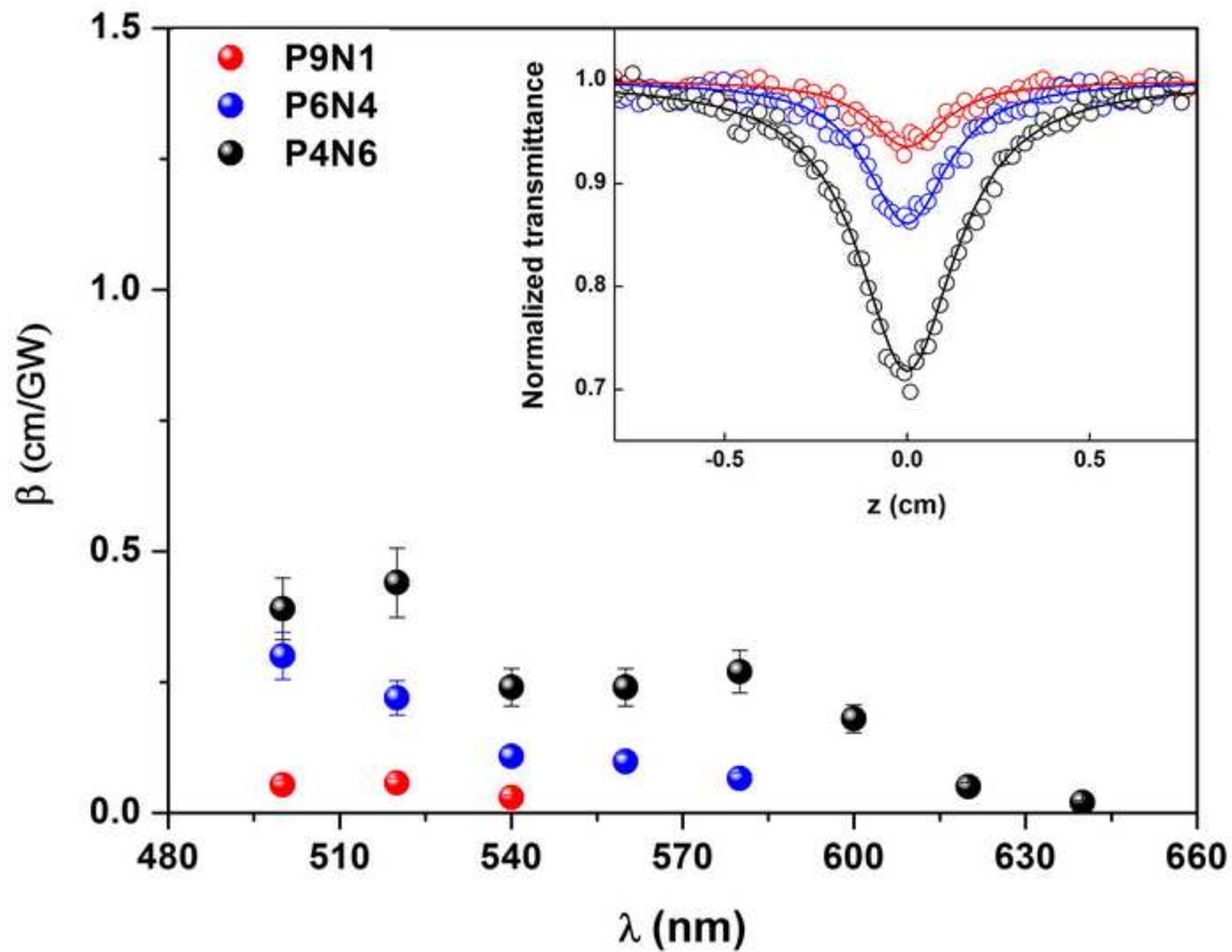


Figure 9

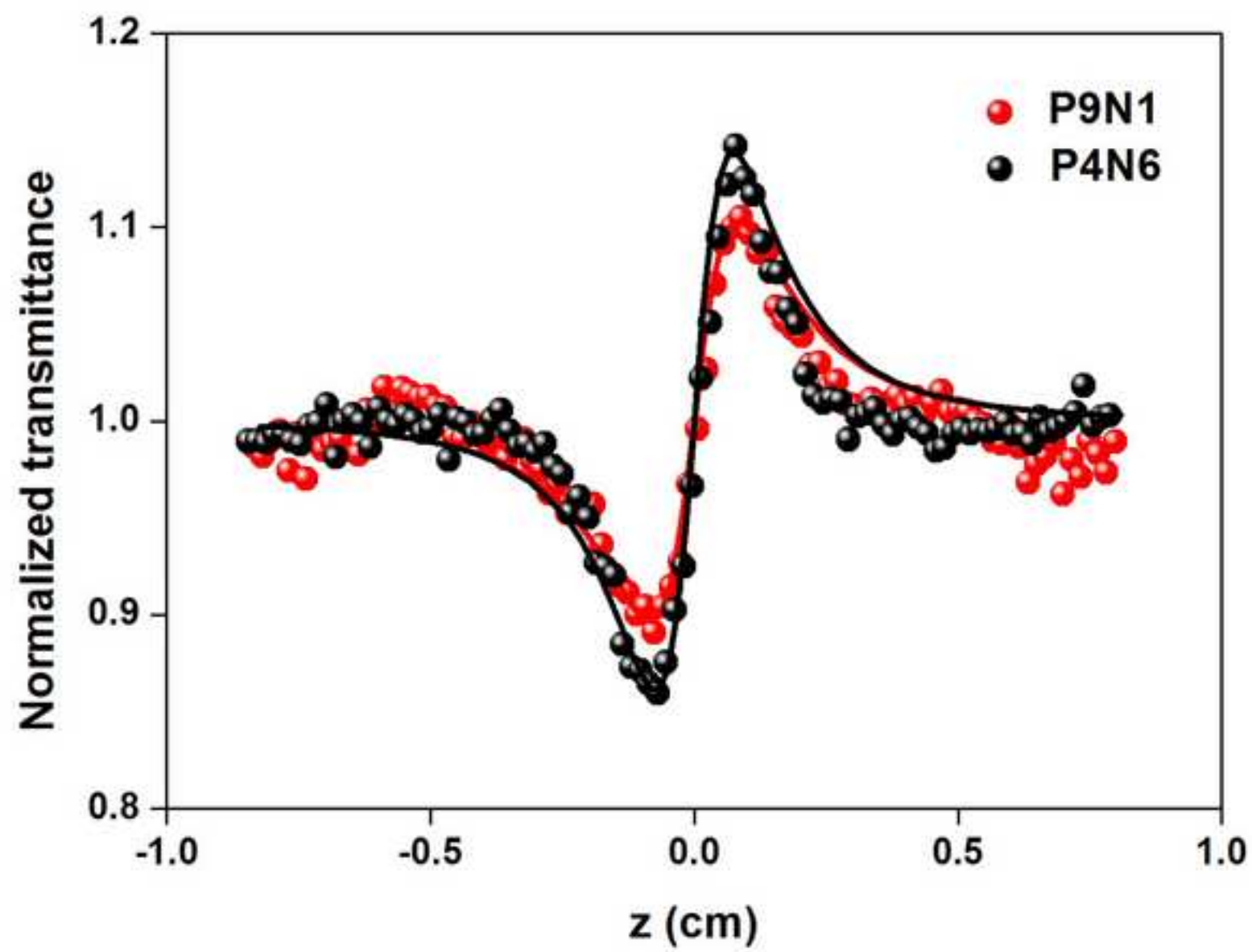


Figure 10

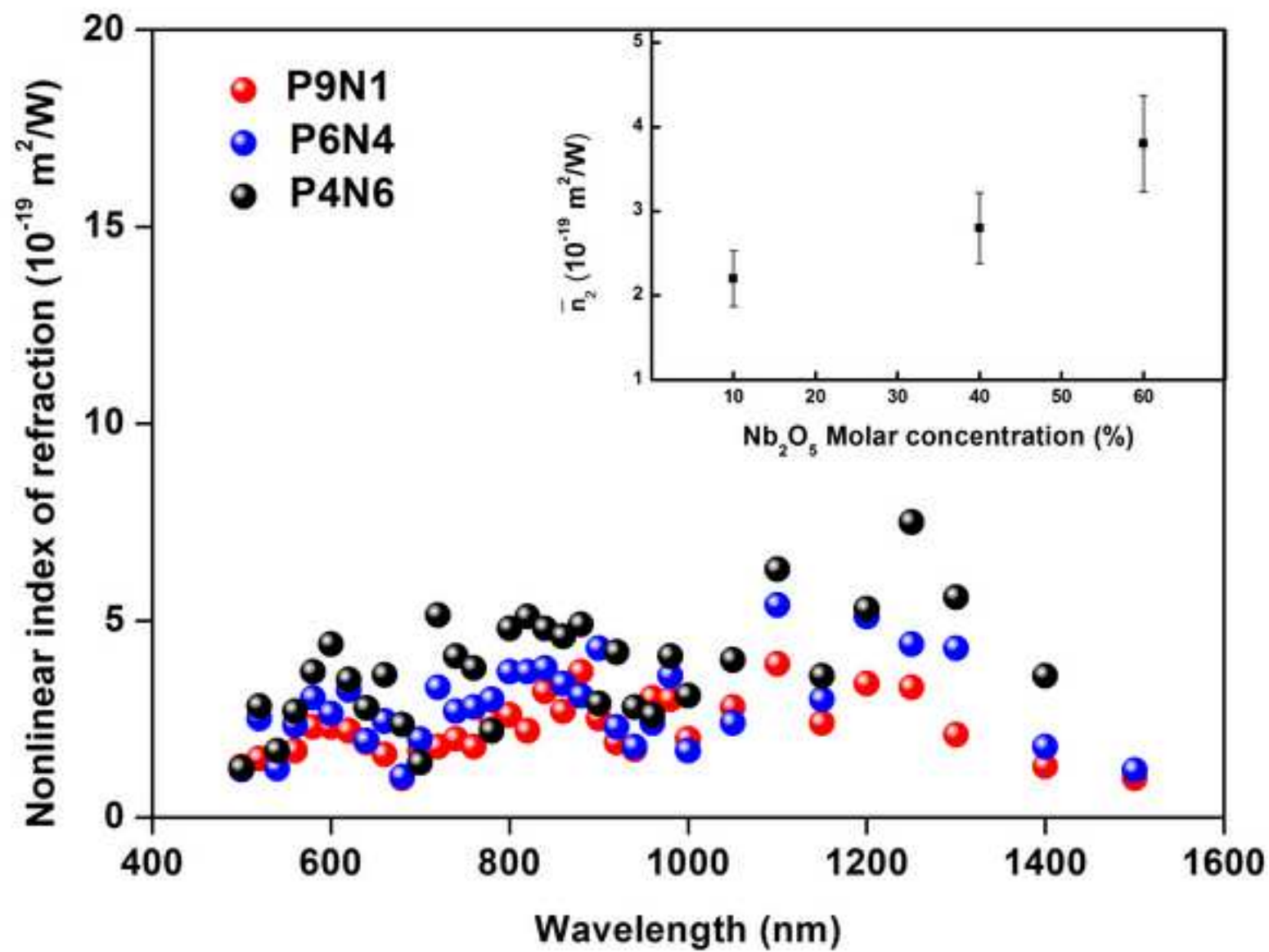


Figure 11

